Chapter 4

An integrated terrestrial-marine landscape evolution model

To facilitate modelling the future evolution of incised coastal gullies, with reference to those found along the south west of the Isle of Wight, it is necessary that both coastal and terrestrial processes are represented in the numerical model used. As explained in chapter 2, Landscape Evolution Models (LEMs) can be used to model terrestrial process interactions. However, the current catalogue of LEMs do not contain any representation of coastal processes. Previously (chapter 3), a simple, processed-based model of cliff retreat has been described and calibrated for the south west Isle of Wight. In this chapter, a description of the unaltered Channel-Hillslope Integrated Landscape Development Model (CHILD; Tucker *et al.*, 2001a,b) is provided, before the modifications required to integrate CHILD with the process model developed in chapter 3 are outlined. Subsequently, details of the parameterisation and validation of the integrated LEM are also provided.

4.1 The Channel Hillslope-Integrated Landform Development Model (CHILD)

As outlined in section 2.5, the Channel-Hillslope Integrated Landscape Development model (CHILD; Tucker *et al.*, 2001a,b) is one of a suite of LEMs capable of representing the terrestrial processes involved in coastal gully evolution over the timescales necessary for the current study. Furthermore, the run times involved are considerably quicker than alternative models (see figure 2.12). For detailed information into the computational workings of CHILD see Tucker *et al.* (2001a,b), as only brief descriptions of the underlying process mechanisms are provided below. An outline of the major functions and their interactions is shown in figure 4.1.

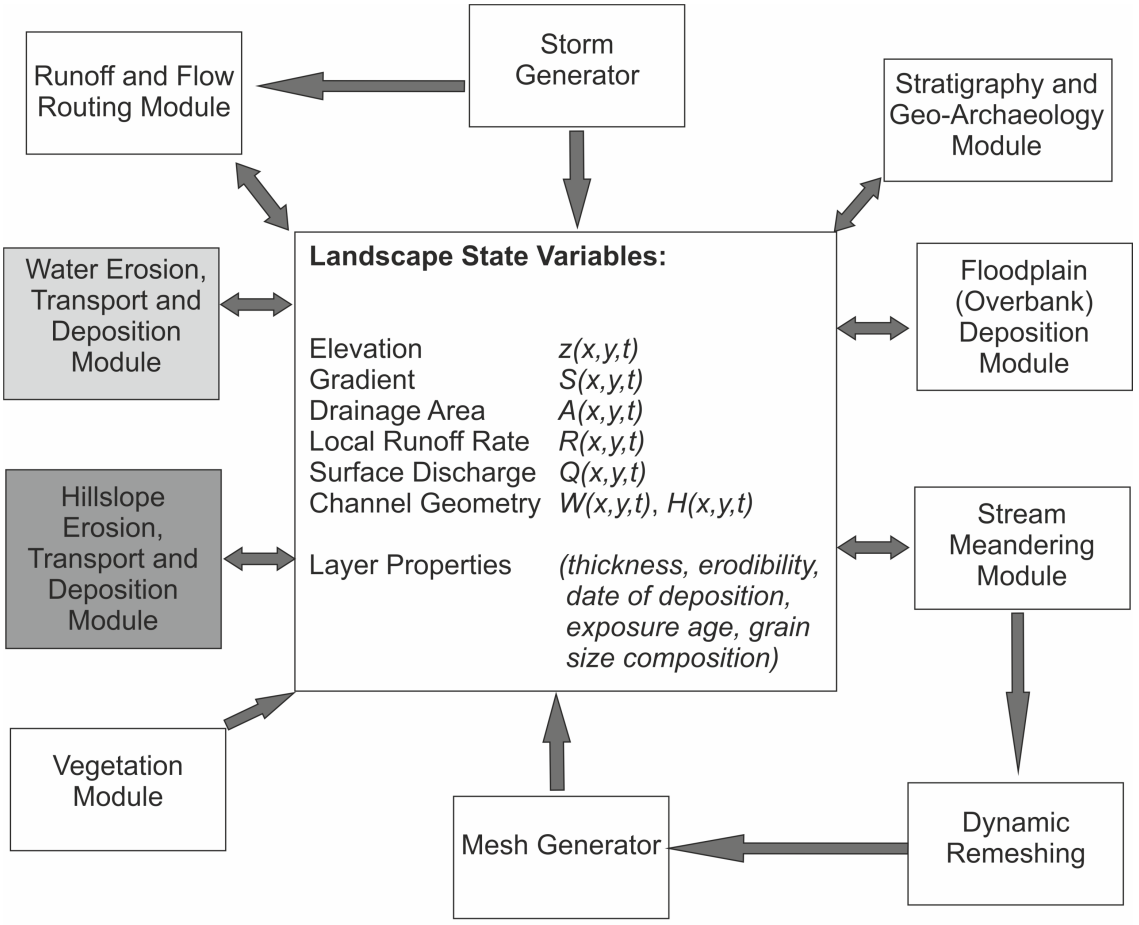

FIGURE 4.1: Overview of the components in the CHILD model. The state variables W and H represent channel width and channel depth, respectively. CHILD iterates through a discrete series of storm and interstorm periods (see section 4.1.3. for further details regarding the temporal framework of the model). Components in light grey are updated only after every storm event, components in dark grey are updated after every interstorm period whist components in white are updated after both storm and interstorm periods (if the option for these components is selected). Adapted from Tucker et al. (1997).

4.1.1 Spatial framework

CHILD simulates landscape evolution by modelling the passage of water and sediment across a landscape surface discretised as an irregular mesh of interconnecting triangles, a framework known as a Triangular Irregular Network (TIN; Braun and Sambridge, 1997). The use of a TIN offers several key advantages over models based on a regular grid;

1. The resolution of the model can vary in space, allowing features of interest (e.g. gully networks), or areas of complex terrain (e.g. gully sidewalls), to be represented in higher levels of detail (Tucker *et al.*, 2001a,b).

2. The spatial resolution can be adjusted dynamically in response to changes in the rates and nature of processes occurring at a node (Braun and Sambridge, 1997; Tucker *et al.*, 2001a,b).

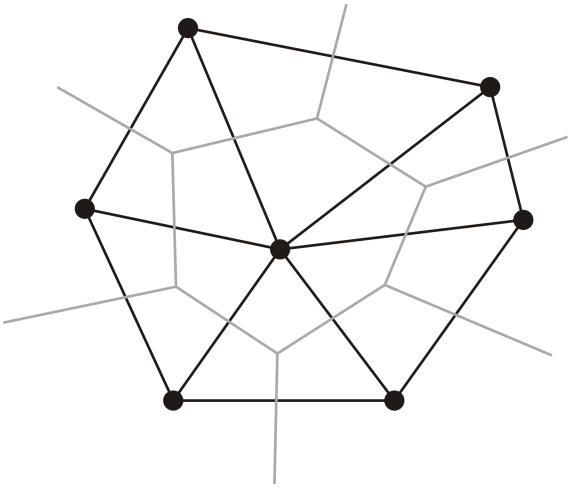

FIGURE 4.2: Schematic illustration of CHILD model mesh elements. Nodes (points) are identified by the solid black circles. The Voronoi cell is symbolised by the grey lines. The edges of the TIN cell are symbolised by the black lines. Adapted from Tucker et al. (2001,2001a).

3. Nodes can be moved horizontally as well as vertically, which makes the simulation of lateral and surface-normal erosion (e.g. meandering channels and cliff retreat) possible (Tucker *et al.*, 2001a,b), allowing complex gully and cliff features to develop.

4. Nodes can be added to simulate lateral accretion of features such as point bars and cliff-toe slumps (Tucker *et al.*, 2001a,b).

5. The mesh can be coupled with 3D kinematic models of tectonic deformation, thus simulating interactions between topography and crustal deformation (Tucker *et al.*, 2001a,b).

The set of nodes representing the landscape are connected using Delaunay triangulation (figure 4.2). Delaunay triangulation produces a unique set of triangles that connect a set of points in such a way that a circle passing through three points of a triangle will contain no other points. Each node, N_i, is associated with a Voronoi Cell (figure 4.2), the region within which any arbitary point would be closer to N_i than to any other node on the grid. In CHILD the Delaunay triangulation defines the connectivity between the adjacent nodes, whilst the Voronoi Cell defines the surface area of each node (Tucker *et al.*, 2001a,b).

4.1.2 Continuity of mass

As with all LEMs, changes in elevation are described by the continuity of mass equation

$$\frac{\delta z}{\delta t} = -\nabla q_s + U(x, y, t) \tag{4.1}$$

where z is elevation, t is time, q_s is the sediment flux (bulk volume per unit width) and U is a source term representing uplift at location (x, y) at time t.

CHILD solves Eq.4.1 by treating each Voronoi Cell (figure 4.2) as a finite-volume cell (Braun and Sambridge, 1997; Tucker *et al.*, 2001a,b; Peió and Sherwin, 2005). Thus for each node, Eq.4.1 can be written as

$$\frac{\delta z_i}{\delta t} = \frac{1}{\Lambda_i} \sum_{j=1}^{M_i} Q_{Sji} \tag{4.2}$$

where z_i is the elevation of node i, M_i is the number of nodes connected to node i and Q_{Sji} is the total volumetric sediment flux from node j to node i (negative if flux is from node i to node j). Total local sediment flux is then computed based on a series of laws for each of a set of discrete landscape sediment transfer processes, defined further in section 4.1.4.

4.1.3 Temporal framework

The temporal framework of any landscape evolution model ideally needs to address one of the major challenges of modelling terrain evolution, that of the disparity between the time scales of topographic change (e.g. years to geologic epoch) and the time scales of storms and floods (e.g. minutes to days; Tucker and Bras, 2000; Tucker *et al.*, 2001a). In previous models this had been addressed through the use of constant climatic variables (e.g. Willgoose *et al.*, 1991; Howard, 1994; Tucker and Slingerland, 1994). Although this approach is computationally efficient, the use of constant climatic variables means it fails to account for the effects of climate variability on erosion and deposition (Tucker and Bras, 2000). Additionally, it fails to acknowledge the stochastic dynamics which occur when a variety of events of differing magnitude and frequency occur in the presence of geomorphic and hydrological thresholds (Tucker *et al.*, 2001a).

To address these issues the time step between model iterations within CHILD may be controlled by a stochastic rainfall model outlined by Tucker and Bras (2000). The model alternates between periods of 'storms' and 'interstorms' based on the Poisson rainfall model of Eagleson (1978). Each 'storm' has constant rainfall intensity, P (m/yr), duration, T_r (yr), and interstorm duration, T_b (yr). For each storm event, these three parameters are chosen at random from exponential probability distributions (Tucker *et al.*, 2001a,a). This method allows for climate variables to be based on observed climate statistics (Tucker and Bras, 2000) whilst also allowing for variations in climate, such as storm frequency and magnitude, to be modelled. Furthermore, this method means no limits are places on the timescales over which CHILD may operate, the only limit is that the run must be longer than one storm event (Tucker *et al.*, 2001a).

Alternatively P, T_r and T_b may be kept uniform, in which case the mean values are

applied throughout the whole model run (thus the duration of each iteration is $\bar{T_r} + \bar{T_b}$). This approach represents that of previous models (e.g. Willgoose *et al.*, 1991; Howard, 1994; Tucker and Slingerland, 1994). In either case, each storm event has a constant storm intensity throughout its duration, and this assumption is also applied to the resulting hydrograph (Tucker *et al.*, 2001a,b).

Time variant fluctuations and perturbations in climate can be represented by utilising the inbuilt *tTimeSeries* function. This function makes CHILD read an input file as a time series and allows parameters such as P, T_r and T_b to adjust with time. This facilitates the assessment of transient changes in future precipitation climates, by allowing parameters downscaled from Global Climate Models to force the climate components of CHILD.

As a consequence of the stochastic temporal framework of CHILD, transport and erosional processes driven by runoff are only computed during storm periods. Not only is this computationally efficient, but it is also logical, in that it is storms which perform the majority of geomorphic work and are the driver of sediment transport and erosion.

4.1.4 Process representation

CHILD simulates a range of geomorphic erosion and transport functions, grouped into modular families of functions in figure 4.1. Some of these functions (e.g. Stream Meandering, Stratigraphy and Geo-archaeology) are not required for this study and so will not be described here. Details of modules and functions used in this study are provided below in brief. For information on all the modules in CHILD see Tucker *et al.* (2001a,b) and Clevis *et al.* (2006).

4.1.4.1 Hillslope transport

Continuous hillslope sediment transport, such as soil creep, is represented within CHILD using two alternative formulations. Firstly a linear model of the form

$$q_c = K_d \nabla \cdot z \tag{4.3}$$

where q_c is volumetric sediment discharge per unit width, K_d is a transport coefficient (L^2/T) and z is elevation, following Culling (1963).

Secondly, a non-linear model of Roering *et al.* (1999, 2001), taking the form

$$q_c = \frac{K_d \nabla \cdot z}{1 - (\frac{|\nabla \cdot z|}{S_c})^2} \tag{4.4}$$

where S_c is a threshold slope gradient at which the transport rate tends to infinity.

The linear equation represented in Eq.4.3 fails to account for large-scale mass wasting processes. However, in Eq.4.4 sediment flux tends to infinity as S_c is approached, therefore landsliding and large-scale mass-wasting are able to be represented in the non-linear model (Roering *et al.*, 1999, 2001). The process of landsliding has been shown to occur by using Eq.4.4 in experimental hillslope experiments when the critical gradient exceeds 0.5 (Roering *et al.*, 2001). As the processes of mass wasting and landsliding are important to the evolution of gully side walls (Leyland and Darby, 2008), Eq.4.4 is used in this study.

It is worth noting here that wash is not included in the hill slope process category, rather it is lumped in with channel erosion. This has the advantage of simplicity, however wash erosion is effectively treated as a sub-set of rill erosion in which rills have the same hydraulic geometry as larger channels (Tucker *et al.*, 2001a,b).

4.1.4.2 Fluvial erosion

CHILD includes several fluvial transport formulae, which describe both transport- and detachment-limited erosion of sediment. Transport-limited systems refer to those in which sediment transport flux is limited by the capacity of the river to transport sediment. Conversely, detachment-limited systems assume that the river can transport an infinite amount of sediment, and that the sediment flux is limited only by the capacity of river to detach material from the river bed. Detachment-limited erosion is normally applied to bedrock channels or landscapes with thin regolith layers. As discussed in chapter 2, the incised coastal gullies of the Isle of Wight have low sediment yields, predominantly made up of fine material. As such, they may be described as detachment limited systems. However, in CHILD each cell has a regolith and bedrock depth, only in cells where the regolith has been eroded away and the bedrock exposed will detachment limited erosion be applied. Therefore it is necessary to include representation of both transport- and detachment-limited erosion. Accordingly, a description of both sets of transport formulae is provided below and the most appropriate formulation within each sub-set is identified. A summary of each model included within the CHILD model is given in table 4.1.

4.1.4.2.1 Transport limited erosion

CHILD contains seven transport-limited transport equations. Each is briefly described below before a summary of the available models is provided. Functional forms of each equation are provided in table 4.1.

$Power - law\ formula,\ form1.$
Here transport-capacity, Q_c, is estimated based on an excess shear-stress model of the

form

$$Q_c = K_f W(\tau_0 - \tau_c)^{P_f} \tag{4.5}$$

where, K_f is a transport efficiency factor (m^3/s per unit excess stress), W is the channel width (m), τ_0 is bed shear stress (Pa), τ_c is critical shear stress required for erosion (Pa) and P_f is a user-defined exponent. This model is based on the Meyer-Peter and Muller (1948) sediment transport equation.

Power − law formula, form 2.
In this form, the exponent of Eq.4.5, P_f is applied to the stress and threshold terms separately, rather than putting the exponent outside the parentheses. Thus,

$$Q_c = K_f W(\tau_0^{P_f} - \tau_c^{P_f}) \tag{4.6}$$

where $\tau_c^{P_f}$ can be represented in terms of a shear stress (when P_f =1) or in terms of a unit stream power (when $P_f = \frac{3}{2}$). In the second case, $\tau_c^{P_f}$ is proportional to the critical unit stream power needed for entrainment, and the coefficient terms relating to velocity and shear stress are subsumed into K_t. Tucker (2004) claims there is little reason to favour Eq.4.5 over this form (Eq.4.6) of the power-law formula, which is easier to solve and dimensionally consistent.

The modified Bagnold formula of BridgeandDominic(1984).
The Bridge and Dominic (1984) bedload formula is based on the Bagnold (1966) equation of sediment transport. The form as implemented in CHILD is

$$Q_B = K_f W(\tau - \tau_c)(\sqrt{\tau} - \sqrt{\tau_c}) \tag{4.7}$$

where Q_B is bedload. This model uses a simple polynomial form from which an analytical solution can be directly obtained (Tucker, 2004). This model is included in CHILD because it is expected that the bedload fraction will tend to control the stream gradient because of its larger entrainment threshold (Howard, 1980; Tucker, 2004).

A two fraction sand and gravel model developed by Wilcox (1998) *and Wilcox* (2001).
This formulation represents the two-fraction model of Wilcox (1998) and Wilcox (2001). The two grain-sizes represented are sand and gravel. The model represents the transport capacity of each fraction, as described by Gasparini *et al.* (1999, 2004, 2008), such that

$$\begin{aligned} Q_{cg} &= \frac{11.2 W f_g}{(s-1)g}\left(\frac{\tau}{\rho}\right)^{1.5}\left[1 - \frac{\tau_{cg}}{\tau}\right] \\ Q_{cs} &= \frac{11.2 W f_s}{(s-1)g}\left(\frac{\tau}{\rho}\right)^{1.5}\left[1 - \frac{\tau_{cs}}{\tau}\right] \end{aligned} \tag{4.8}$$

where Q_{cg} is the transport capacity of gravel, Q_{cs} is the transport capacity of sand, f_g is the proportion of gravel on the bed, f_s is the proportion of sand on the bed, s is the ratio of sediment density to water density (ρ), g is gravitational acceleration and τ_{cg} and τ_{cs} are the critical shear stress values for gravel and sand, respectively, and 11.2 is a dimensionless parameter (Gasparini *et al.*, 2004).

A generic power − law formula for multiple grain size fractions.
This option is a Meyer-Peter Muller-like transport formula capable of representing up to nine grain-size fractions. The transport capacity of each grain-size fraction, i, is given by

$$Q_{ci} = f_i K_i W(\tau_0 - \tau_{ci})^{P_f} \tag{4.9}$$

where f_i is the proportion of grain-size i on the bed and τ_{ci} is the effective critical shear stress for the i-th grain size fraction.

The sand − gravel formula of WillgooseandRiley(1998).
Willgoose and Riley (1998) incorporate a transport capacity model able to model the erosion of sand and gravel into the LEM SIBERIA (Willgoose *et al.*, 1991). This model has subsequently been incorporated into CHILD. This model follows the form

$$Q_c = \beta_1^{'} q^{m_1^{'}} S^{n_1^{'}} (\tau - \tau_c) \tag{4.10}$$

where the parameters $\beta_1^{'}$, $m_1^{'}$, and $n_1^{'}$ are fixed by the flow cross-section geometry and erosion physics. The parameter $\beta_1^{'}$ provides the rate of sediment transport and is analogous to the parameter K used in previous models.

A simple slope − discharge power law.
A simple power law relationship of the form

$$Q_c = K_f Q^{m_f} S^{n_f} \tag{4.11}$$

following Howard and Kerby (1983) is included in CHILD. Here, m_f and n_f are the exponents of discharge (Q) per unit width and slope (S), respectively. It is worth noting that Eq.4.11 does not include a threshold term, or a link to the shear stresses generated on the river bed.

A summary of transport capacity laws.
The above equations enable the calculation of transport capacity under a wide range of transport and bed substrate conditions. For application to the incised coastal gullies of the Isle of Wight, those equations relating to multiple grain sizes (Eqs.4.8, 4.9 and 4.10) can be excluded, as the sediment composition of the incised coastal gullies of interest here can be well idealised as single grain size material, more specifically fine sands (Flint, 1982).

The simple stream power law presented in Eq.4.11 assumes steady, uniform flow, in detachment-limited conditions (Howard and Kerby, 1983; Berlin and Anderson, 2007). It is unlikely that flow in the incised coastal gullies of the Isle of Wight will be steady and uniform, given their high gradient and the flashy nature of their hydrograph. Therefore, the applicability of this model is questionable. Furthermore, Stock and Montgomery (1999) note that Eq.4.11 is best applied in areas with stable base levels. As such, the incised coastal gullies of the Isle of Wight, which constantly undergo changing base levels due to the processes of cliff retreat and sea level rise, may be ill-suited to this model.

The remaining three equations (Eqs.4.5, 4.6 and 4.7) all contain a threshold shear stress component. Models involving basal shear stresses have been shown to be applicable to small catchments composed of homogenous material similar to the incised coastal gullies of the Isle of Wight (Tomkin *et al.*, 2003; Crosby and Whipple, 2006), therefore all three threshold shear stress models are valid for this environment.

Tucker (2004) argues that there is no clear reason to distinguish between Eqs.4.5 and 4.6. Clearly, differences exist between the two forms, especially when τ is close to τ_c. However, the uncertainty regarding the applicability of differing sediment transport laws is larger than the potential inaccuracy introduced by selecting Eq.4.6 over Eq.4.5 (Tucker, 2004). Tucker (2004) then goes on to compare Eq.4.6 and Eq.4.7; he concludes that the non-linear effects introduced by the application of a threshold shear stress have a strong impact on the morphology and dynamics of an eroding landscape. It was found that Eq.4.6 maintains higher gradients at lower transport rates than Eq.4.7, whilst Eq.4.7 produced smoother stream profiles over large timescales. As steep channel gradients and stepped stream profiles (characterised by a series of knickpoints) are key morphological features of incised coastal gullies (Leyland and Darby, 2008), the maintenance of these features is required if future models of incised coastal gully development are to be representative of current, observed, forms. It was therefore decided that Eq.4.6 shall be used within CHILD to represent the transport-limited erosion of sediment.

4.1.4.2.2 Detachment limited erosion

Further to the seven transport-limited formulae described above (see table 4.1), CHILD also incorporates two detachment-capacity equations which may be used to model bedrock erosion. Both these equations calculate detachment capacity as a power of shear stress above a threshold. A brief outline of each law is given before a summary is provided. Functional forms of each formula are provided in table 4.1.

$Power - law$, $form$ 1.
In this form, a simple power law describing detachment-capacity, D_c, as a function of excess shear stress is formulated following Howard and Kerby (1983), such that

$$D_c = K_{br}(\tau - \tau_c)^{P_b} \tag{4.12}$$

Model	Functional Form	Source
1. Power Law, Form 1	$Q_c = K_f W(\tau_0 - \tau_c)^{P_f}$	Meyer-Peter and Muller (1948)
2. Power Law, Form 2	$Q_c = K_f W(\tau_0^{P_f} - \tau_c^{P_f})$	Meyer-Peter and Muller (1948), Tucker (2004)
3. Modified Bagnold Formula	$Q_B = K_f W(\tau - \tau_c)(\sqrt{\tau} - \sqrt{\tau_c})$	Bridge and Dominic (1984)
4. Two-Fraction Sand and Gravel Formula	$Q_{cg} = \frac{11.2 W f_g}{(s-1)g}\left(\frac{\tau}{\rho}\right)^{1.5}\left[1 - \frac{\tau_{cg}}{\tau}\right]$	Wilcox (1988, 2001), Gasparini et al. (1999, 2004, 2008)
	$Q_{cs} = \frac{11.2 W f_s}{(s-1)g}\left(\frac{\tau}{\rho}\right)^{1.5}\left[1 - \frac{\tau_{cs}}{\tau}\right]$	
5. Generic Power Law for Multiple Grain Sizes	$Q_{ci} = f_i K_i W(\tau_0 - \tau_{ci})^{P_f}$	Based on Meyer-Peter and Muller (1948)
6. Sand and Gravel Formula	$Q_c = \beta_1^{'} q^{m_1^{'}} S^{n_1^{'}}(\tau - \tau_c)$	Willgoose and Riley (1998)
7. Simple Slope-Discharge Formula	$Q_c = K_f Q^{m_f} S^{n_f}$	Howard and Kerby (1983)
8. Power Law, Form 1	$D_c = K_{br}(\tau - \tau_c)^{P_b}$	Meyer-Peter and Muller (1948)
9. Power Law, Form 4	$D_c = K_{br}(\tau^{P_b} - \tau_c^{P_b})$	Meyer-Peter and Muller (1948), Tucker (2004)

TABLE 4.1: Functional forms of the seven transport capacity laws (1 to 7) and the two detachment-capacity laws (8 and 9) in CHILD.

where K_{br} is a rate coefficient, τ_c is a threshold below which no detachment takes place and P_b is a user defined exponent equal to 1 if τ_c is to be represented as a shear stress, or $\frac{3}{2}$ if τ_c is to be equated to a critical unit stream power (Tucker, 2004).

Power − law, form 2.
In this form, the exponent of Eq.4.7, P_b, is applied to the stress and threshold terms separately, rather than putting the exponent outside the parentheses such that

$$D_c = K_{br}(\tau^{P_b} - \tau_c^{P_b}) \tag{4.13}$$

following Tucker (2004).

Summary of detachment − limited laws.
As with the argument pertaining to Eq.4.5 and 4.6 above, there is no clear reason to distinguish between equations 4.12 and 4.13 (Tucker, 2004). The uncertainties induced by selecting Eq.4.13 over Eq.4.12 are negligible (Tucker, 2004). Furthermore, Eq.4.13 is more analytically tractable than Eq.4.12 and has been used in previous studies of long term landscape evolution (Tucker, 2004). Therefore, in this study Eq.4.13 is used to calculate detachment-capacity sediment transport.

4.2 Modelling coastal erosion in a landscape evolution model

As previously discussed, no existing LEM includes processes of coastal erosion. Indeed, as stated by Tucker and Hancock (2010), there is a need for creative solutions to modelling cliff retreat in LEMs. This problem has, in this research, been tackled by developing a module which can be integrated into the pre-existing CHILD code. By utilising the relationships between accumulated excess energy (AEE) and net shoreline movement (NSM) developed in chapter 3, it is possible to represent processes of coastal erosion within the existing CHILD LEM framework. The concept for this module is outlined in figure 4.3.

As stated by Istanbulluoglu *et al.* (2005), most LEMs make no allowance for vertical steps in the landscape (e.g. cliff faces and gully head-cuts) and purely horizontal motion of such features (e.g. coastal erosion). This issue is also raised by Tucker and Hancock (2010) in their review of the state of LEMs. Similarly to the U-shaped gullies modelled by Istanbulluoglu *et al.* (2005), cliffs represent distinct discontinuities within the landscape, marking a sudden break of slope. As cliff retreat is often directed normal to the cliff face along the horizontal plane, the identification of cells located on a cliff face is important.

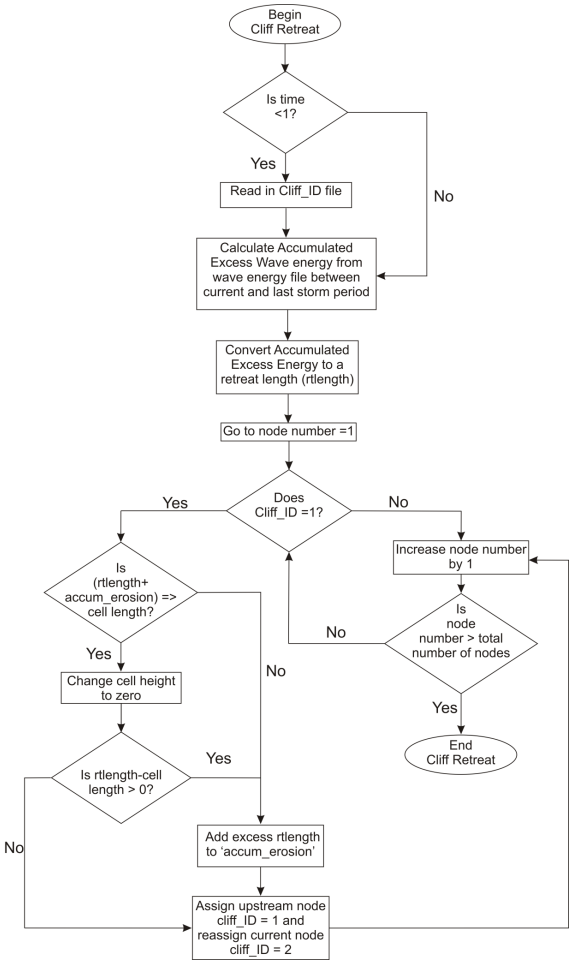

FIGURE 4.3: Flow chart showing the implementation of the marine cliff retreat module.

In the routine described below, the identification of marine cliff[1] nodes is contained within a separate input file, this file contains the x- and y-coordinates of nodes located on a marine cliff, as well as a marine cliff ID (0 = not cliff, 1 = cliff, 2 = eroded cliff cell). These IDs are determined from slope and aspect analysis in ArcGIS, however could be manually defined by the user through the use of polygon masks to delineate areas of marine cliffs. With reference to the incised coastal gullies of the Isle of Wight, marine cliff cells are defined as cells whose aspect is south to southwest (157.5° to 247.5°) and whose slope is 30° or over. The steep sided and sinuous nature of incised coastal gullies means that automatic identification of marine cliff cells, based on the slope and aspect criteria described above, within CHILD or GIS packages, such as ArcGIS, still results in many cells located along the gully sidewalls being identified erroneously as marine cliff cells. This subsequently results in coastal processes being applied to areas of the gully which are normally solely affected by terrestrial processes. It is, therefore, necessary for the user to manually remove ID tags erroneously identified as marine cliff cells, after the automatic identification routine has been implemented.

[1]The distinction between marine and non-marine cliffs is made here to distinguish between cliffs which may be found within the gullies themselves and are not under the influence of marine processes and those which are created through marine processes.

During every storm period within the model, the AEE between the current and previous storm periods is calculated from hourly significant wave height and sea level records (H_T), read in from a separate input file containing the hour (as a fraction of the year) and a respective H_T value. The nature of this method allows for the assessment of transient future changes to wave climate and sea level on coastal erosion processes. This AEE value is then converted to a length of retreat (m), *rtlength*, from the relationships developed for the specific geological Cliff Units in the Isle of Wight in chapter 3 (figure 3.14). For the whole Isle of Wight coast this relationship can be expressed as

$$rtlength = \left([6.90 \times 10^{-7} \times \Sigma(\Omega - \Omega_c)\right) + 0.918 \tag{4.14}$$

where Ω is wave energy (J/m^3) and Ω_c is a threshold wave energy (J/m^3).

If a node has a marine cliff ID of 1, the *rtlength* calculated for the current time step is compared to the length of the cell. If the cell length is less than or equal to *rtlength* then the whole cell is assumed to be eroded to baselevel. The excess retreat, (*rtlength* - cell length), if any, is stored in the variable *accum_erosion* and carried over to the next iteration where it is added to the subsequent time-step's *rtlength*. If the cell length is greater than *rtlength* the value of *rtlength* is stored in *accum_erosion* and similarly carried over to the next iteration. This method allows for variation in cell size and allows differential erosion along the coastline, in places where cell sizes may vary. It also preserves the values of erosion calculated and makes sure the whole erosion event is accounted for.

Once a marine cliff cell has been eroded, the marine cliff ID assigned to that node is passed to the cell directly upslope. This ensures that the vector of retreat is directed inland. Subsequently, the eroded node is assigned a marine cliff ID of 2 to show it is an eroded cliff cell. This allows for visualisation of the coastal erosion process as well as keeping track of previous marine cliff lines. The modified CHILD code was termed Marine-Terrestrial CHILD (MT-CHILD). This terminology will be used henceforth to distinguish between the modified and unmodified code.

4.2.1 Cliff retreat code verification

To verify that the integrated cliff retreat module, when fully integrated into the MT-CHILD LEM, does not result in erroneous outputs and does not affect modules already integrated in the LEM, a grid of 100 x 100 nodes, with a spacing of 10 m was generated in Matlab (see figure 4.4a). One side of the grid was set as an open boundary, allowing sediment to leave the system if transported to this edge. A cliff face was initially located at y = 100. This framework also makes sure that the vector of cliff retreat was directed inland.

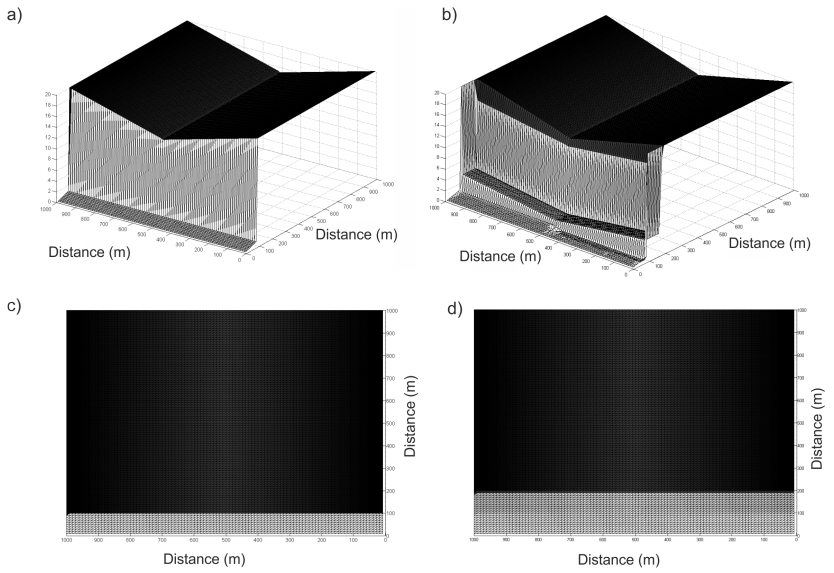

FIGURE 4.4: Implementation of the cliff retreat module in MT-CHILD. a) initial DEM in isometric view, b) after 100 years in isometric view, c) plan view of initial DEM, d) plan view of DEM after 100 years. Model was run with wave climate of 1995 replicated 100 times to represent a constant $0.9 ma^{-1}$ retreat rate.

As this run was not designed to test the fluvial and hillslope interactions with the coastal retreat function, the mean storm intensity, duration and interstorm period were set to arbitrarily chosen values of 10.6 m/yr, 0.0009 yrs (7.9 hours) and 0.08yrs (29 days) respectively. The erosional/depositional parameters were set as described in section 4.3.1 below.

The calibration period for the coastal retreat module outlined in chapter 3 covered the period 2001 - 2011. Therefore, to test the cliff retreat module using a different data source than that used for its calibration, the wave regime of the Channel Light Vessel in 1995 was used in this experiment. The 1995 wave record was replicated 100 times to provide a simulated 100 year record of hourly significant wave heights. The accumulated excess energy above the threshold wave height defined for the Isle of Wight (6.2 m; see figure 3.14a) equates to a retreat length of 0.9 ma^{-1} when calculated through the linear relationship described in figure 3.14a (Eq. 4.14). Therefore by replicating this yearly record 100 times, a total retreat of 90 m is expected. As can be seen in figure 4.4 (b and d) the change in cliff position corresponds to a change of 90 m, therefore the model replicates the appropriate change in cliff position. Furthermore, figure 4.5 demonstrates the models ability to maintain realistic cliff profiles throughout the simulation.

4.3 Validation of the cliff retreat module

In order to test the validity of the cliff retreat module described above, MT-CHILD was parameterised for the incised coastal gullies found along the south west Isle of Wight as

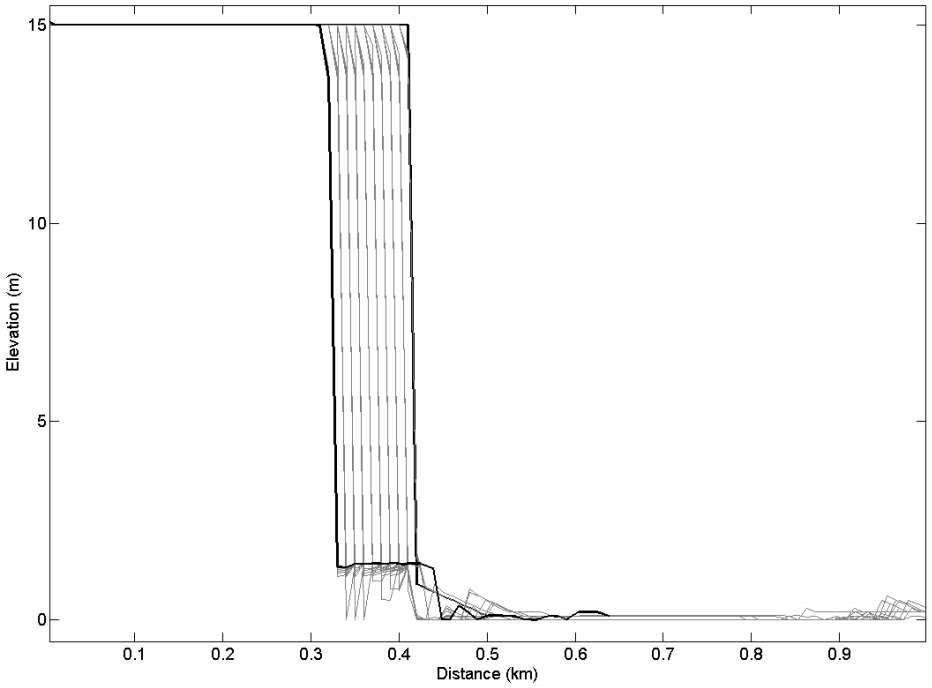

FIGURE 4.5: One dimensional profiles showing the evolution of a cliff. Each profile corresponds to a change in profile over time during the simulation. The thick black lines relate to the start (right hand bold line, y=100 in figure 4.4 c) and finish (left hand bold line, y = 190 in figure 4.4 d) profiles.

described below (section 4.3.1). MT-CHILD was applied to Shepherds Chine, Isle of Wight, over the time period 1810 - 2009 (see section 4.3.2). A series of plausible historical drivers were developed from observed records to be used as inputs into the simulation (section 4.3.3).

4.3.1 Parameterisation of MT-CHILD

This section outlines the model parameters used to set MT-CHILD up to model the incised coastal gullies of the Isle of Wight. The coastal retreat module detailed in section 4.2 utilised the general parameters values applied to the whole of the landscape. As such, the parameters described below are applied to the whole landscape. The coastal retreat module only requires specific driving conditions, which are detailed below in section 4.3.2.

4.3.1.1 Alluvial erosion

It has been shown previously (chapter 2) and in previous research (Leyland and Darby, 2008, 2009) that the incised coastal gullies are predominantly bedrock features. As such, the movement and removal of regolith from these systems is not considered as important as the erosion of bedrock. However, the removal of regolith in the upper reaches of the

catchment signifies the extension of the incised coastal gully's system and represents the headwards erosion of the channel network. As described above (section 4.1.4.2.1) transport-capacity is estimated in MT-CHILD using the Tucker (2004) version of the excess shear stress power law (Eq.4.6). The efficiency parameter k_f was set to maximum efficiency (a value of one), as little regolith is contained within the incised coastal gully systems, suggesting they are highly efficient at removing regolith material. Channel width (m), W, is estimated from discharge according to the power-law hydraulic geometry equations of Leopold and Maddock (1953) such that

$$W = k_w Q^{w_b} \tag{4.15}$$

where k_w is the hydraulic width coefficient, Q is discharge and w_b is the hydraulic width exponent. Values of the exponent, w_b, have been shown to vary in natural channels between 0.3 and 0.5 (Montgomery and Gran, 2001), however, the commonly accepted value for this exponent is 0.5 (Leopold and Miller, 1956; Wharton *et al.*, 1989; Rodriguez-Iturbe and Rinaldo, 1997; Montgomery and Gran, 2001; Wohl, 2004). For application to the incised coastal gullies of the Isle of Wight, the commonly assumed value of 0.5 is used.

The value for threshold critical shear stress, τ_c, in Eq.4.6 was calculated by Leyland and Darby (2008) for the two dominant geologies found along the south west Isle of Wight; the Wealden Shales and Marls and the Lower Greensands. They used a cohesive strength meter (CSM) following the methods of Tolhurst *et al.* (1999) to determine the shear stresses required to initiate erosion of the bedrock. It was found that the threshold shear stress for the Wealden Shales and Marls was double that of the Lower Greensands at 3.6 $\pm$ 0.5 Nm^{-2} and 1.8 $\pm$ 0.3 Nm^{-2} respectively (where these values represent the mean $\pm$ one standard deviation of multiple CSM replicates).

4.3.1.2 Bedrock erosion

As discussed in section 4.1.4.2 bedrock erosion in MT-CHILD is modelled using Eq.4.13. To replicate the dynamics of the incised coastal gullies of the south west Isle of Wight, the bedrock erodibility coefficient K_{br} is set to 0.015 following Leyland and Darby (2008, 2009). Following Howard (1994), Whipple and Tucker (1999) and Attal *et al.* (2008), the rate of bedrock erosion is considered proportional to the rate of energy dissipation per unit bed area. Consequently, the parameter P_b is set to $\frac{3}{2}$. The values for critical shear stress are the same as those described above for fluvial erosion (section 4.3.1.1).

Parameter	Units	Value
Fluvial Erosion		
K_f - regolith transport efficiency	-	1
K_w - hydraulic width coefficient	-	10
W_b - hydraulic width exponent	-	0.5
τ_{cr} - critical shear stress (Wealden Shales and Marls)	Nm^{-2}	3.6
τ_{cr} - critical shear stress (Lower Greensands)	Nm^{-2}	1.8
Bedrock Erosion		
K_{br} - bedrock erodibility coefficeint	$\mathrm{L}^{1-2m}/\mathrm{T}$	0.015
P_b - critical shear stress exponent	-	1.5
τ_{cr} - critical shear stress (Wealden Shales and Marls)	Nm^{-2}	3.6
τ_{cr} - critical shear stress (Lower Greensands)	Nm^{-2}	1.8
Hillslope Erosion		
K_d - hillslope diffusivity coefficient	ma^{-1}	0.01
S_c - critical slope for mass wasting	m/m	0.75

TABLE 4.2: Summary of CHILD parameter values used.

4.3.1.3 Hillslope processes

The diffusivity coefficient of Eq.4.4, K_d, is set to 0.01 m^2a^{-1}, this value has been shown to be suitable for the incised coastal gullies of the Isle of Wight, and also for incised marine terraces in the United States (Rosenbloom and Anderson, 1994; Tucker and Slingerland, 1997; Leyland and Darby, 2008, 2009). The threshold slope gradient, S_c, is set to 0.75 m/m derived from direct measurements of gully sidewalls (Leyland and Darby, 2008, 2009). Although gully sidewall slopes vary along the gully course, following the Channel Evolution Model (CEM) proposed by Leyland and Darby (2008), the value of 0.75 m/m is suitably high enough to encapsulate the maximum observed slope and ensure mass-wasting and landsliding processes are induced using the non-linear hillslope Eq.4.4 (Roering *et al.*, 1999, 2001).

The gully catchments are likely to be affected by slow diffusive processes, however over the time period in question (∼100 years) this process is unlikely to have much of an effect on overall landscape evolution. Conversely, the processes of mass wasting and landsliding are likely to play a large role in the evolution of the incised coastal gullies over the ∼100 year time frame of this project (Leyland and Darby, 2008, 2009).

A summary of all the parameters detailed above and used in the set-up of MT-CHILD is given in table 4.2.

4.3.2 Sherpherds Chine simulation

To test the interaction between the terrestrial and coastal processes within the modified model, MT-CHILD was set up to replicate the development of Shepherds Chine.

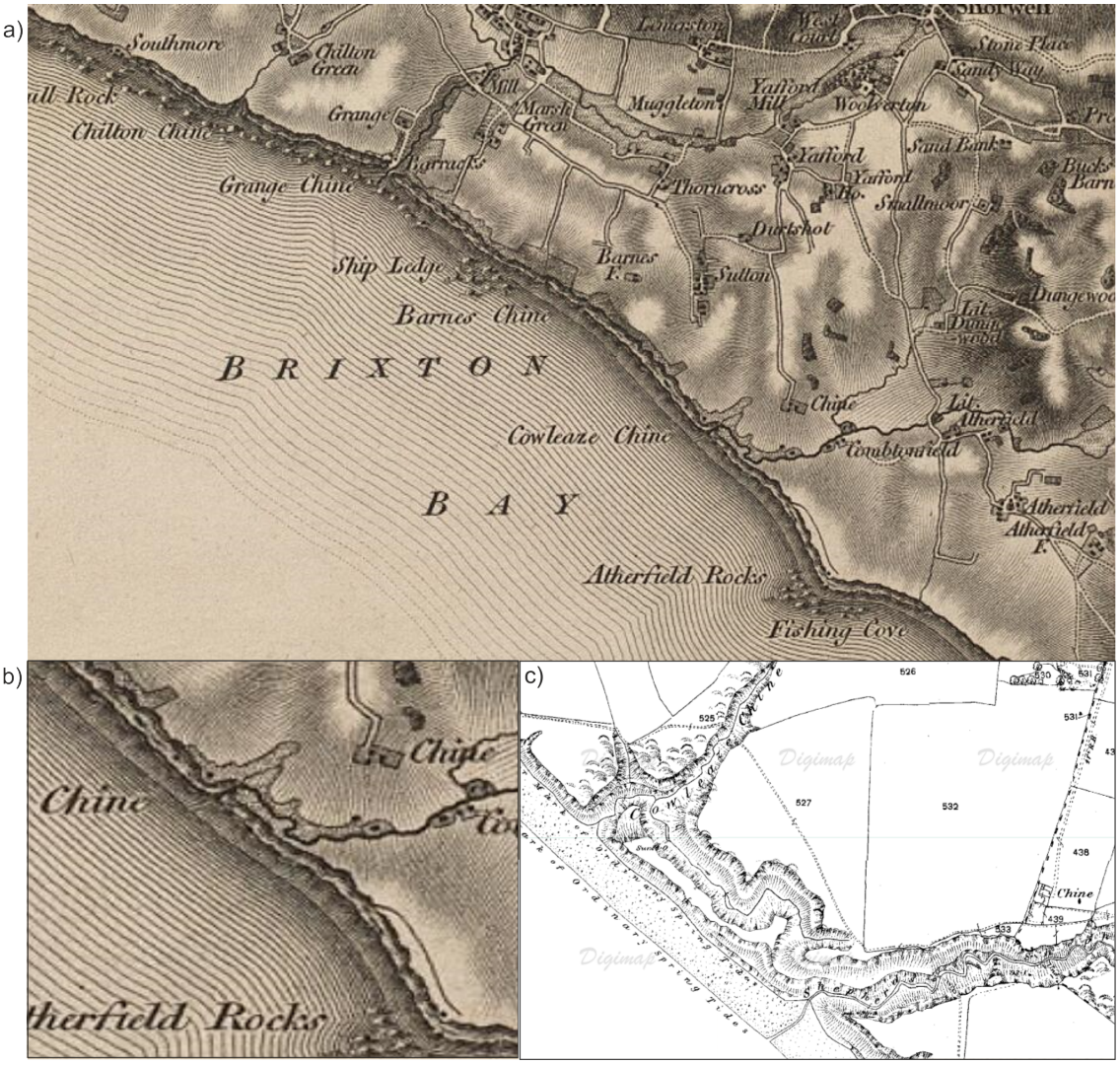

FIGURE 4.6: Ordnance Survey map from 1810 (first edition). b) Close-up of Cowleaze and Shepherds Chine from Ordnance Survey map from 1810, showing Chine stream flowing through Cowleaze Chine. c) Ordnance Survey map from 1862 showing how the formation of Shepherds Chine has captured the stream and breached the cliffs to flow to into the English Channel.

Shepherds Chine is formed in the Wealden Shale geology, at the southern end of the south west Isle of Wight coastline (figure 1.1). It has a contributing drainage area of 11.3 km^2, making it the second largest Chine by catchment area on the Isle of Wight (Grange/Marsh Chine being the largest with a drainage area of 12 km^2). The length of the present gully is 500 m (measured from Chine mouth to the head-cut of the gully). The width of the Chine at the coast is 180 m, whilst the maximum depth of incision is 25 m. The level of incision at the mouth matches the height of the cliffs, ensuring the stream debouches the gully at base level. Human modification of the Chine is present in the form of an abstraction structure, resulting in the removal of water during low flows. The abstraction license is however regulated to ensure the high flows are left unaffected, as it is these flows that are the most geomorphologically significant, ensuring the Chine is able to develop in a quasai-natural state (Norton *et al.*, 2006).

It is known from historical evidence (Fitton, 1836; White, 1921) that Shepherds Chine has formed since about 1825 (figure 4.6). As shown in historic maps (figure 4.6a, b) the stream previously flowed through Cowleaze Chine to the north. Flint (1982) attributes the diversion of the stream to the digging of a shepherd (hence the name of the Chine), however it is quite likely that the diversion occurred as a result of the cliff retreating back until the stream was able to flow directly out to the English Channel. The rapid incision of Shepherds Chine (∼25 m) over meso-scale timescales (∼190 years) means this catchment is suitable for validating the interactions between the terrestrial and coastal processes within MT-CHILD. Therefore MT-CHILD was set-up and parameterised to recreate the development of Shepherds Chine over the period 1810 to 2009. It must be noted, however, that the model set-up used in this simulation is for a historical initial condition which has subsequently been erased by coastal erosion. This simulation is, therefore, one of retrodicting to match current conditions. Furthermore, the period over which the simulations are run (1810 - 2009) is one of relatively sparse wave and rainfall climate data. This results in a number of assumptions being made in the subsequent model validation process, such that the validation involves a comparison between a plausible model scenario of historical conditions and the observed landforms, not a model of actual historical conditions. Bearing this in mind, the following sections describe the generation of these plausible scenarios of the initial conditions used within the model simulation.

4.3.2.1 Deriving historical landscapes and shoreline positions

The availability of historic maps highlighting the course of the stream prior to the formation of Shepherds Chine (figure 4.6) provides an opportunity to replicate the 1810 landscape of this stretch of coastline. This was achieved by extending the coastal section, defined as the area between the coastline and the half way up the gully channel (figure 4.7), of the combined catchment areas of Shepherds and Cowleaze Chines. The initial digital elevation model (DEM) was derived from 2009 LIDAR data (1 m) and OS Profile data (10 m). The 2009 LIDAR data only covered the extent of the incised gully; therefore OS Profile data was used to model the catchment area of the gully inland of the gully headcut. This combination of data sources allows the more dynamic gully system to be modelled at higher resolution (1 m), whilst saving computational demand by representing the less dynamic and less geomorphically active catchment area of the gully system at a lower resolution (10 m). The coastal section was cut from the initial DEM and the points were moved and aligned to the approximate 1810 position (figure 4.7). This position was estimated from a digitised coastline from the 1810 Ordnance Survey first edition map (see figure 4.6a) and subsequent 1863 revision.

The hinterland area behind the headcut of the Chine was left the same as the present day. This was done to ensure the drainage area of the gully was preserved and thus the correct amount of water was routed through the gully system. The altered coastline

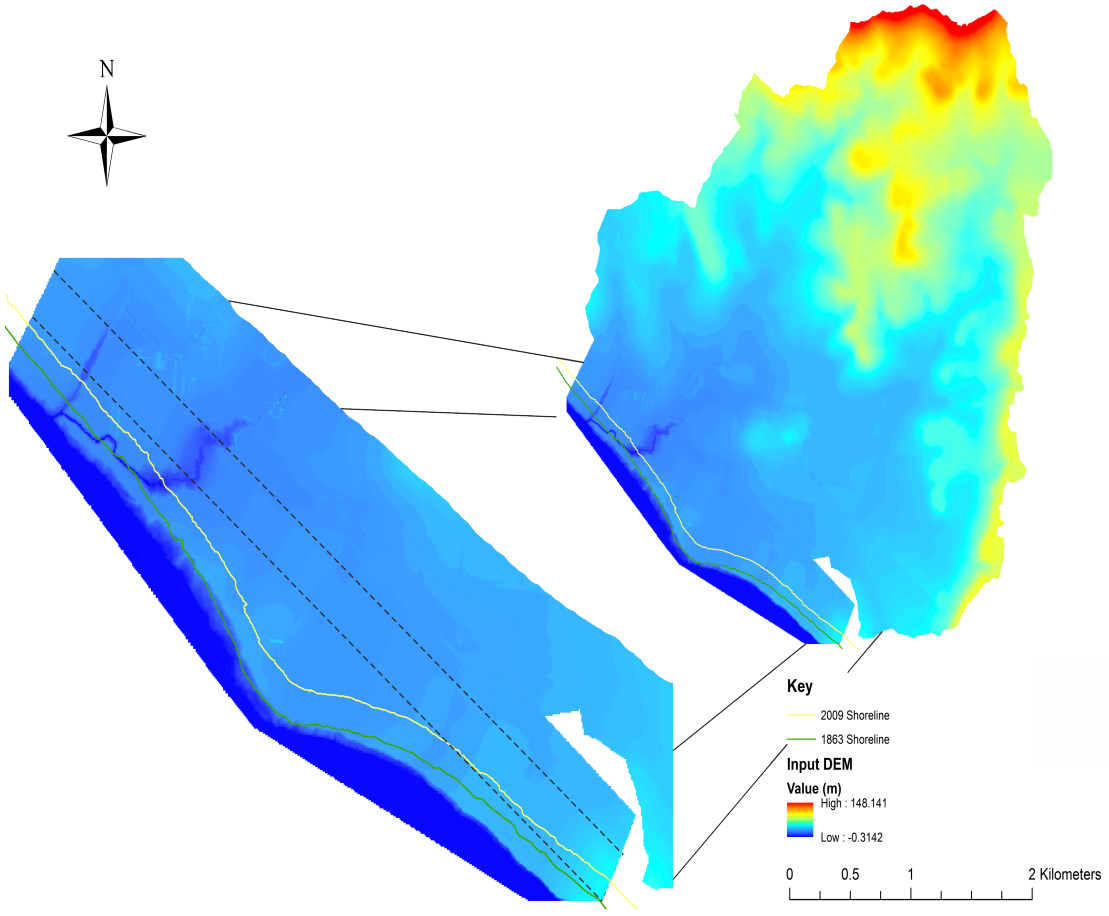

FIGURE 4.7: Synthetic digital elevation model (DEM) of Shepherds Chine in 1810 derived from LIDAR and OS profile data. Shorelines for 1863 and 2009 show how far the DEM has been extended. The area enclosed by the dashed black lines on the inset delineates the area which has been extended and interpolated. The area to the left of the left-hand dashed line is the coastal section of the gully which was cut and moved. Scale bar relates to the large catchment wide DEM only.

section of the DEM was then re-interpolated using a nearest neighbour technique with a grid cell size of 5 m. A channel, of dimensions approximate to that of the 1810 gully channel as derived from historic map evidence, was manually cut through the DEM to ensure the flow from Shepherds Chine was diverted to Cowleaze Chine in the north before reaching the coast (figure 4.7). Flow accumulation and direction was checked in ArcGIS to ensure the flow was routed along the correct course.

As well as the initial landscape for the model (derived from historical map evidence), a plausible series of historical rainfall and wave heights are needed to run the model over the 199 year study period.

4.3.2.2 Developing historical daily rainfall data

As mentioned in section 4.1.3 MT-CHILD requires inputs of mean storm intensity (ma^{-1}), mean storm duration (years) and mean interstorm duration (years). These

parameters can be made to vary through time using the *tTimeSeries* function (see section 4.1.3), thus allowing MT-CHILD to model observed trends in precipitation.

It is common for records of daily or sub-daily rainfall for the period 1810 to 2009 to be sparse, if not non-existent. For the area in question, sub-daily resolution rainfall data is available from the Met. Office weather station at St. Catherine's Point (∼6 km south of Cowleaze and Shepherds Chine) for the period 1961 to present. Alexander and Jones (2001) provide a daily record of rainfall for the south east of England using Met. Office MIDAS data which covers the period 1931 - 2011. Additionally, historical monthly total precipitation has been recorded over the period 1855 - 2000 at Southampton. As none of these available data sources extend far enough back to cover the whole period required, it is necessary to extend one of these records through the use of proxy data sources or statistical modelling. As such, the rainfall series used in the model validation process is only one of a series of possible rainfall scenarios, and does not represent actual historical rainfall. The generated rainfall series is checked to ensure it is within the natural variability captured in observed rainfall records for this region, however it must be stressed that the series is a best guess representation of observed rainfall. With these caveats in mind, keeping the temporal resolution of the data at a useful scale (daily) whilst providing enough data to account for events of a large return period is of key importance. Therefore, the daily resolution south east England record of Alexander and Jones (2001) was chosen.

It has been shown that the Generalised Pareto distribution (GPD) can be used to model series of daily precipitation (Van Montfort and Witter, 1986; Coles, 2001; Coles *et al.*, 2003; Su *et al.*, 2009). In fact, Su *et al.* (2009) show that the GPD is better at modelling daily precipitation than the Generalised Extreme Value, General Logistic and Wakeby distributions. The GDP is a right-skewed distribution and the probability density function of the GPD with shape parameter $k \neq 0$, scale parameter σ and threshold parameter θ is given by

$$y = f(x|k, \sigma, \theta) = \left(\frac{1}{\sigma}\right)\left(1 + k\frac{(x-\theta)}{\sigma}\right)^{-1-\frac{1}{k}} \tag{4.16}$$

for $\theta < x$, when k 0, or for $\theta < x < \frac{\sigma}{k}$ when $k < 0$.

The GPD was fitted to the daily rainfall data for the period 1931 - 1990. As the threshold parameter, θ, is user-defined in the GPD, visual inspection of the fit to probability plots was conducted with different threshold parameters. It was found that the best fit was produced when θ = -1.2 (figure 4.8a). Following this, maximum likelihood estimates of k and σ were 0.11 (Std. error = 0.006) and 2.82 (Std. error = 0.026) respectively. To test the validity of this fit, the 20 year period from 1990 to 2010 was used as a validation series. A random series was generated according to the GPD fit. The statistics describing the observed data between 1990 and 2010 and the modelled

	Observed Data (mm)	Modelled Data (mm)
Minimum	0	0
Maximum	41.96	43.43
Mean	2.07	1.98
Median	0.3	0.8
Standard Deviation	3.81	3.58

TABLE 4.3: Descriptive statistics of observed daily rainfall series between 1990-2010 and modelled daily rainfall series over the same period.

data set are presented in table 4.3. It can be seen that the modelled data displays a similar mean and standard deviation to the observed data.

The maximum value produced by the model (43.43 mm) exceeds the maximum in the observed data (41.96 mm); however the difference between maximums (1.47 mm) is less than one standard deviation of the observed data, suggesting that the value is within the natural variability recorded within the observed rainfall record. Therefore, it can be said that the model suitably predicts the large, extreme values in precipitation which are important for this study. Furthermore, the residuals between the observed and modelled data sets (figure 4.8d) suggest no systematic over- or under-prediction by the GPD model. This is confirmed by the mean of the residuals, -0.08, which suggests a slight under estimation. This slight underestimation is also displayed in the total precipitation modelled by the GPD (14.45 m), which is consistent with the total precipitation observed over the same period (15.1 m) and which represents and underestimation of 0.03 m a year.

It has been shown that the GPD can satisfactorily model precipitation over the validation period (1990 - 2010). Thus, a random data series covering the period which daily resolution data are not available (1810 to 1931) was then generated using the validated model parameters (k = 0.110453, σ = 2.9001 and θ = -1.2). This was then combined with the observed data covering the period 1931 to 2009 to provide a daily rainfall record for the whole period in question. To test if the synthesised rainfall record portrays a viable simulation of historic rainfall, daily rainfall levels were accumulated into monthly totals and compared to the 1855 - 2000 monthly rainfall record from Southampton (figure 4.9a). A ten year moving average was calculated as it has been observed that there are large decadal fluctuations in storm occurrence over decadal scales (Alexandersson *et al.*, 1998; Bärring *et al.*, 2004; Hanna *et al.*, 2008; Wang *et al.*, 2009; Donat *et al.*, 2011).

Comparison of the two records suggests that decadal variations in rainfall are replicated in the modelled rainfalls series. A Pearsons correlation coefficient of 0.66 ($p < 0.05$) suggests that the two records correspond to each other, further highlighting that decadal fluctuations are represented in the modelled series. Furthermore, the total amount of observed rainfall over the period 1855 - 2000 was 107.72 m, whereas the modelled total

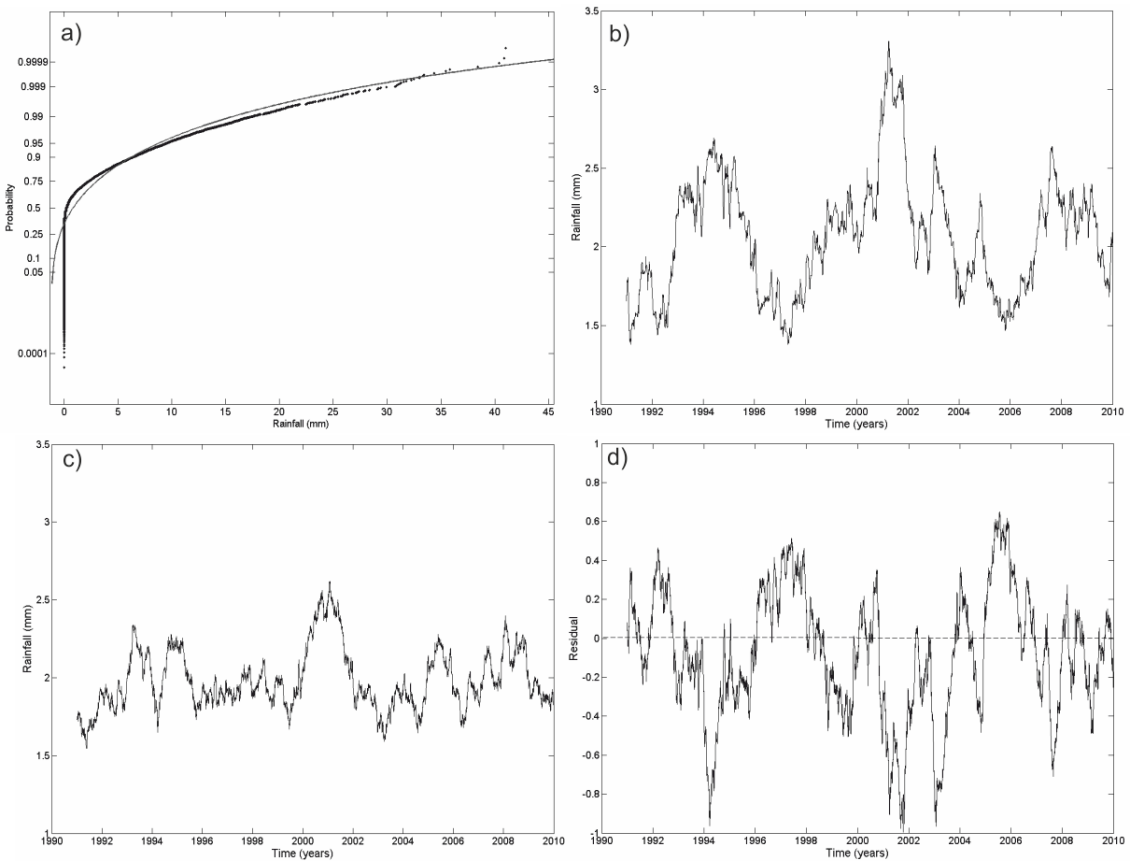

FIGURE 4.8: Analysis of the fit of the GPD to observed daily rainfall data from 1990 to 2010. a) Probability plot for the best fit model (θ = -1.2, k = 0.110453 and σ = 2.9001). Observed data is represented by the black dots. The probability distribution function of the GPD is represented by the solid grey line. b) Yearly moving average of observed rainfall data between the period 1990 and 2010. c) Yearly moving average of the modelled data set over the period 1990 to 2010. d) Residuals between the observed yearly moving average (b) and the modelled yearly moving average (c).

rainfall over the same period was 108.25 m. An overestimation equating to 0.004ma^{-1}. Additional analysis of the residuals between the two rainfall series (figure 4.9b) suggests no systematic over- or under- estimation, however the mean residual value (0.68) suggests an over-estimation.

Figure 4.9b shows that the largest periods of over-estimation correspond to periods of relatively low observed monthly rainfall totals (∼1900 and ∼1950, figure 4.9b). It appears that the GPD over-estimates, predominantly, periods of lower rainfall totals. As the over-estimation displayed in the residuals is not manifested in the total rainfall amount calculated over the 1855-2009 period, this over-estimation balances out over the 145 year period. As it is the larger rainfall events which are important geomorphologically, this over-estimation of lower rainfall totals is considered viable. Furthermore, as the variation in rainfall and total rainfall values are safely in the bounds of the natural variability displayed in the observed rainfall record (table 4.3), the modelled rainfalls series can be said to replicate the observed series and be used as a valid input for this study.

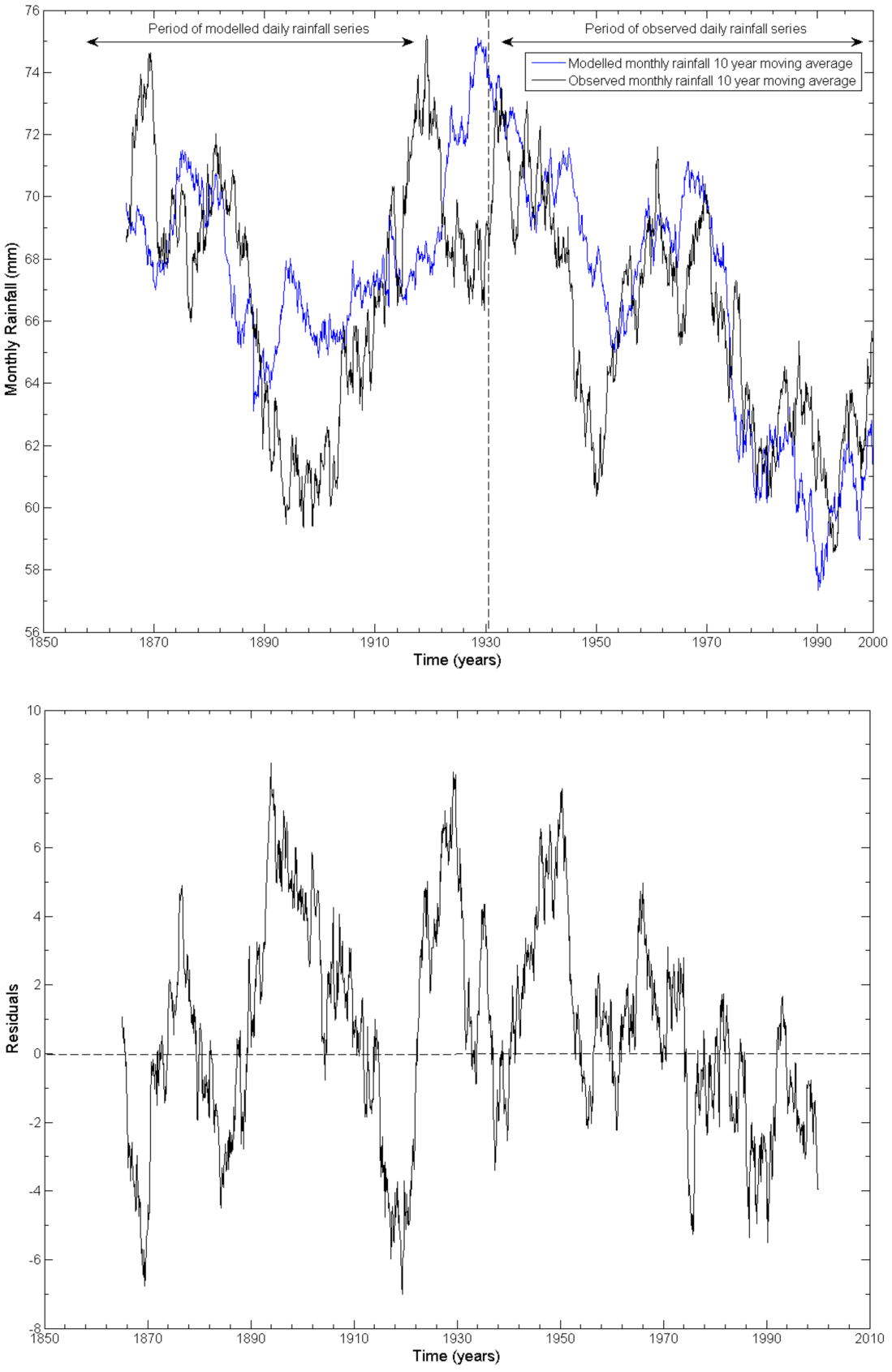

FIGURE 4.9: a) 10 year moving average of monthly rainfall totals from simulated rainfall series (blue) and 10 year moving average of observed monthly rainfall totals from 1855 - 2000 from Southampton, which is located ~35 km from Shepherds Chine (black). b) Residual plot of modelled and observed 10 year moving average total monthly rainfall over the period 1855 - 2000.

4.3.2.3 Developing historical wave climate data

As records of significant wave heights do not exist for the period in question, a time series of significant wave heights (H_s) which span the 199 year period of the validation test also needs to be statistically generated. As discussed in chapter 3, for the Isle of Wight coast, the Channel Light Vessel (CLV) provides the longest record of H_s (1993-2011) and has been shown to represent the wave climate of this coastline during this 19 year period. As it is the extreme values of H_s which provide the energy required for coastal erosion, it is necessary that these are replicated in the synthetic wave climate. Statistical replication of H_s time series has often focused on extremes, either through the modelling of annual maximum data (e.g. Vitousek and Fletcher, 2008), r-largest maxima (e.g. Guedes Soares and Scotto, 2004), peak over threshold (POT) approach (e.g. Goda, 2000) or monthly maxima values (e.g. Panchang and Li, 2006).

The largest problem with the techniques mentioned above is that they assume a homogeneity in the distribution of the population, whereas in reality evidence of seasonality and long term trends in such natural phenomena as wave heights is evident (see figure 4.10; Holthuijsen, 2007; Menéndez *et al.*, 2009; Menendez *et al.*, 2009). Carter and Challenor (1981) and Morton *et al.* (1997) provide two early examples of attempts to model this seasonality. Carter and Challenor (1981) applied a month-to-month distribution, assuming in-month homogeneity, and analysed each month separately. This approach produces twelve distributions, resulting in 36 parameters (if using a three parameter distribution such as the Generalised Extreme Value distribution), which are combined to form an annual model. This approach substantially increases the inherent uncertainty within the overall annual model and thus reduces the validity of such an approach (Menéndez *et al.*, 2009).

More recently, a time-dependent Generalised Extreme Value (GEV) distribution has been applied to block monthly maxima H_s (Menéndez *et al.*, 2009) and sea level heights (Méndez *et al.*, 2007; Menendez *et al.*, 2009; Menéndez and Woodworth, 2010). The time dependent GEV distribution comprises three time dependent parameters, location, $\mu(t)$ < 0, scale, $\psi(t) < 0$, and shape, $\xi(t)$. The GEV distribution includes three distribution families, dependant on the behaviour of the distribution tail. If $\xi(t) = 0$, the tail is light and decays exponentially, so the distribution is of the Gumbel family. If $\xi(t)$ 0, the tail is heavy, decaying polynomially, so the distribution is of the Fréchet family. Finally, if $\xi(t) < 0$, the tail is bounded and so the distribution is of the Weibull family. The cumulative distribution function of the time dependent GEV is thus given by

$$F_t(Z) = \begin{cases} \exp - \left[1 + \xi(t)\left(\frac{z-\mu(t)}{\psi(ti)}\right)\right]^{-\frac{1}{\xi(t)}} & \xi(t) \neq 0 \\ \exp -\exp\left[-\left(\frac{z-\mu(t)}{\psi(t)}\right)\right] & \xi(t) \neq 0 \end{cases} \tag{4.17}$$

where Z represents monthly maxima of significant wave heights, and t is time (years). It

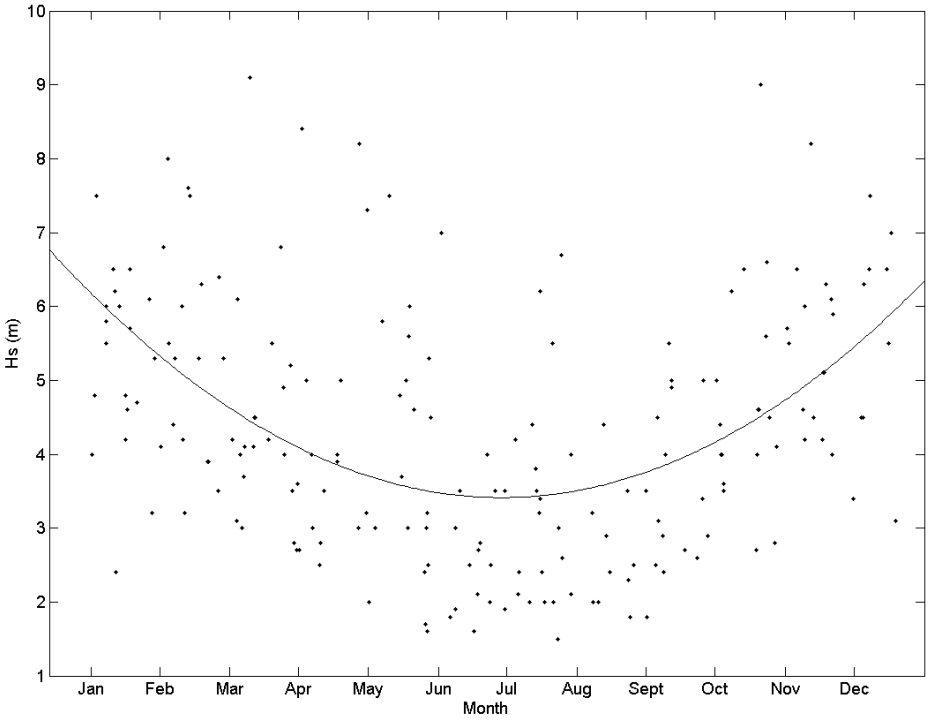

FIGURE 4.10: Scatter plot of monthly maxima significant wave height from the CLV wave buoy between 1990 and 2009. Seasonality in H_s is highlighted by the quadratic trend line, with lower wave heights predominantly occurring during the summer months.

is assumed that the monthly maximum, Z_t, of significant wave heights observed in month t follow a GEV distribution. This assumption is strengthened by visual inspection of the block monthly maxima recorded at the CLV wave buoy between 1993 and 2011, which suggests there is large seasonality within the H_s record (figure 4.10). In general, the larger storm events are experienced in the winter months (Nov - Mar), whilst lower wave heights are experienced over summer mont (June - Aug). This seasonality suggests techniques which rely on the homogeneity of the dataset distribution (e.g. POT or r-largest values) are not well suited to this data, and that the time dependent GEV, which accounts for seasonality, is an appropriate alternative distribution to use.

Following Menéndez *et al.* (2009) the time dependent GEV distribution is fitted to wave data from the CLV from the period 2000 to 2009. As hindcast predictions of possible wave climates are required, the period 2000 to 2009 is used as calibration, with the period 1993 to 1999 used as validation. The time dependent GEV utilises harmonic functions to model the intra-annual variability in H_s. This results in factors detailing annual and semi-annual variations in $\mu(t)$ and $\psi(t)$, whilst a constant value for $\xi(t)$ is maintained throughout. Furthermore, linear trends in $\mu(t)$ and $\psi(t)$ are identified and modelled. These harmonic factors are represented by,

$$\begin{aligned} \mu(t) &= \beta_0 + \beta_1 cos(2\pi t) + \beta_2(2\pi t) + \beta_3 cos(4\pi t) + \beta_4 cos(4\pi t) + \beta_{LT} t \\ \psi(t) &= \alpha_0 + \alpha_1 cos(2\pi t) + \alpha_2(2\pi t) + \alpha_3 cos(4\pi t) + \alpha_4 cos(4\pi t) + \alpha_{LT} t \\ \xi(t) &= \gamma_0 \end{aligned} \tag{4.18}$$

Where β_0,β_1,β_2,β_3 and β_4 are harmonic factors relating to the location parameter, α_0,α_1,α_2,α_3 and α_4 are harmonic factors relating to the scale parameter and γ_0 is the harmonic factor relating to the shape parameter (note the shape parameter has only one factor as this variable is kept constant in the GEV distribution), β_{LT} is the linear trend in the location parameter, α_{LT} is the linear trend in the scale parameter and t is time (in years).

A stepwise algorithm, which combines forwards selection and backwards elimination procedures, is used to fit the best combination of annual and semi-annual factors to the data set. The algorithm tests each factors significance to the overall model before and after new factors have been added, meaning factors already selected may be de-selected if its effects are represented by other factors (see Menéndez *et al.*, 2009, for further details). The criterion for incorporation of a given factor is given by a penalized function based on the Akaike information criterion (Akaike, 1973; Menéndez *et al.*, 2009),

$$AIC_i = -2\ell(\widehat{\theta^i}|t_j, z_j) + 2p_i \tag{4.19}$$

where p_i is the number of parameters, and $\ell(\widehat{\theta^i}|t_j, z_j)$ is the maximum of the log-likelihood resulting from model 'i' for the sample $\{t_j, z_j\}$.

The harmonic factors of the best fit model for the monthly maxima data from the CLV between 2000 and 2009 are detailed in table 4.4, along with their corresponding standard errors and the maximum likelihood estimate (MLE) for the overall time dependent GEV model. To assess whether the best fit GEV parameters describe the wave climate experienced in the English Channel, a random data series covering the period 1993 - 1999 was produced by re-introducing the harmonic factor values (table 4.4) into the GEV distribution parameters detailed in Eq.4.17. Random numbers are then sampled from the GEV distribution with time varying parameters to produce statistically coherent random wave climates for the prescribed period (figure 4.11). Statistics describing the observed and modelled data over the period 1993 - 1999 are displayed in table 4.5. It can be seen that the modelled data displays a similar mean and median value to the observed data set. In addition, the maximum value produced by the GEV distribution is of the same magnitude as the observed data, if slightly over-estimated. However, as the over-estimation is within one standard deviation of the maximum observed value, it is deemed acceptable and within the natural variability displayed by the observed record.

As is shown in figure 4.11a, the yearly moving averages of the observed and modelled series show large differences in their variability. However, the standard deviation of the

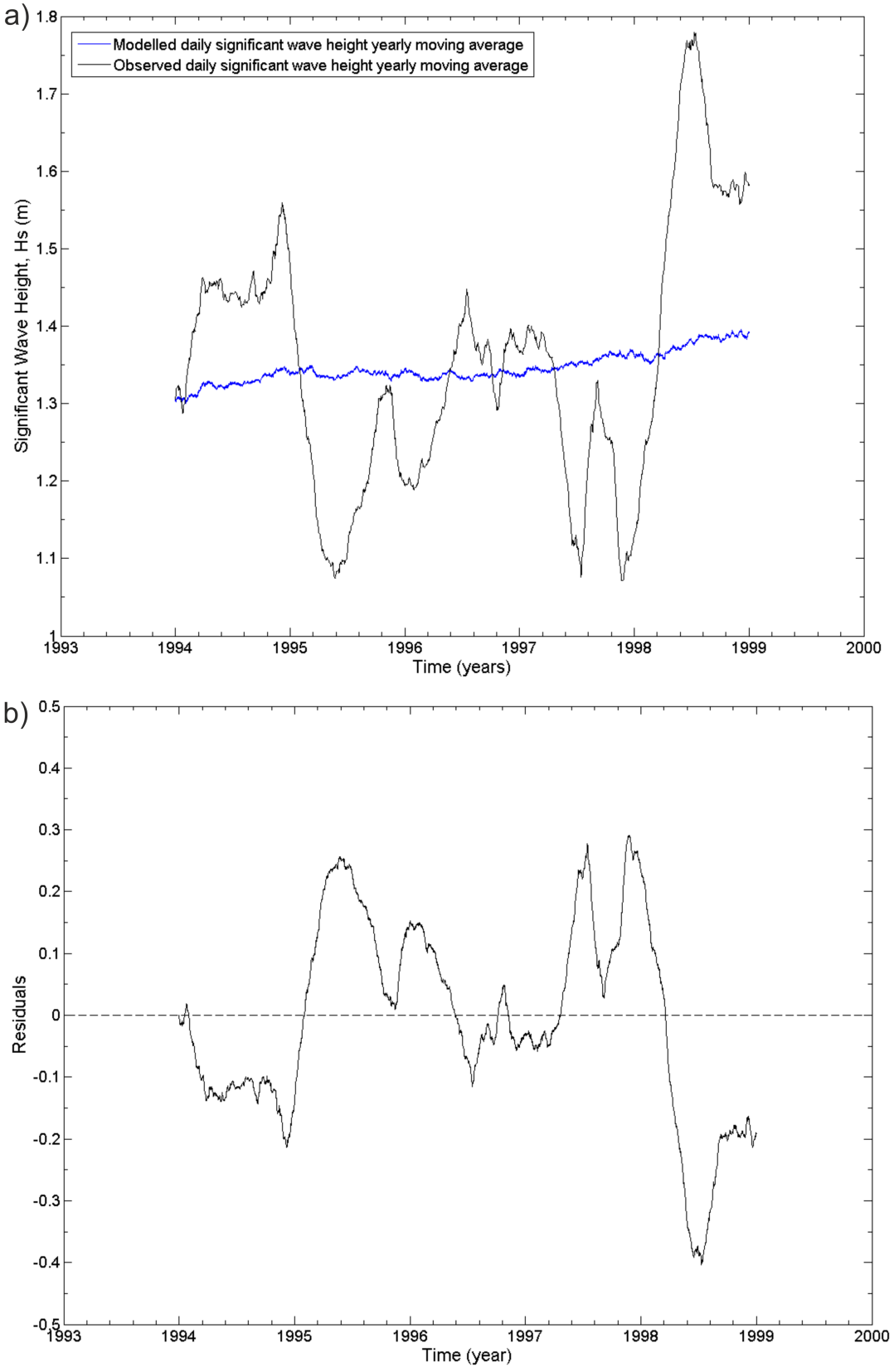

FIGURE 4.11: a) Yearly moving average of observed significant wave height record from the CLV for the period 1993 - 1999 (black) and yearly moving average of the modelled daily significant wave height record derived from the time-variant GEV parameters in table 4.5 (blue). b) Residuals of modelled yearly moving average minus observed yearly moving average for the period 1993 - 1999.

	CLV
β_0	3.629 (0.1027)
β_1	1 (0.0968)
β_2	-0.0032 (0.0541)
β_3	0
β_4	0
β_{LT}	0
α_0	1 (0.1280)
α_1	0.1567 (0.1237)
α_2	0.0391 (0.0938)
α_3	0
α_4	0
α_{LT}	0.0177 (0.1033)
γ_0	0.0177 (0.0122)
MLE	-390.08

TABLE 4.4: Final results of the time depenedent GEV model for the CLV wave buoy with standard errors in parenthesis. The maximum likelihood estimate (MLE) for the model is also given.

modelled data, when not averaged over yearly time scales, is larger than that of the observed data (table 4.5). As the yearly moving average of the modelled data is in the same range as the observed data this is deemed acceptable for this study. Additionally, the residuals of the modelled and observed data (figure 4.11b) suggest there is no systematic under- or over-estimation. The mean of the residuals, -0.01 suggests an ever so slight under-estimation within the modelled data. However, as this value is negligible the model is deemed to accurately represent the variability in the observed wave climate. The maximum variability observed in the residuals is -0.4, as this value is safely within the natural variability of the observed data this is deemed suitable for this study. Overall, analysis of the residuals and comparative statistics of the modelled and observed data series, it appears the time-dependent GEV distribution, when parameterised with the values in table 4.4, is able to suitably represent the variability and extremes in observed wave climates. Therefore, a longer modelled series was produced to cover the study period of 1810 - 1993. This was adjoined to the observed wave climate from the CLV for the period 1993 - 2010 to produce a plausible historic wave climate scenario for input into the modified CHILD model (figure 4.12).

To test the validity of the synthetic wave record produced, the historic atmospheric pressure record from Jersey and Guernsey, Channel Islands, UK (Hanna *et al.*, 2008) over the period 1848 to present was compared to the wave height record (figure 4.12). Pressure changes have long been used as a proxy for storminess in the North Atlantic (Putins, 1962; Schmith *et al.*, 1997). Periods of high pressure are associated with periods of fewer, less severe storms and subsequently, lower wave heights. Conversely, periods of low pressure result in more intense storm activity and therefore result in higher wave

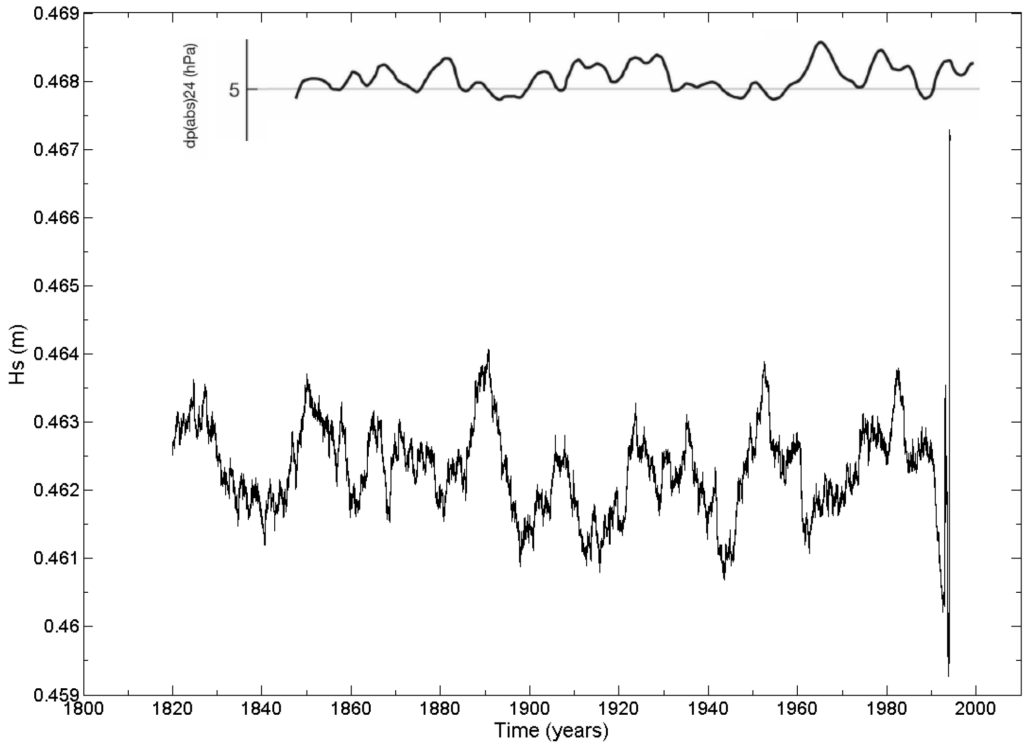

FIGURE 4.12: 10 year moving average of 200 year wave climate from the time-dependent GEV distribution whose parameters are detailed in table 4.4 for the period 1810 - 1993 and observed wave climates from the CLV for the period 1993 - 2010. Inset is Hanna et al. (2008) pressure change (dp(abs)24, hPa) record for Jersey, acting as a storminess proxy for the English Channel. Data begins and ends 10 years earlier and later than actual series because of the nature of the 10 year moving average window. The spike in mean wave height in the 1990s represents the transition from modelled to observed data, a change in mean wave height of 0.002 m is present between the two data sets.

heights (Hanna *et al.*, 2008). As can be seen in figure 4.12, the synthesised long-term wave record displays periods of quiescence and intensity over similar periodicities as those identified in the pressure change record. For example, the period between 1960 and 1970 is characterised by a peak in the Hanna *et al.* (2008) pressure record and a corresponding lull in the mean wave heights. Similarly the 1890s and 1950s correspond to low pressure periods in the Hanna *et al.* (2008) record, and higher mean average wave heights. It can be said, therefore, that the generated wave record represents a plausible wave climate for the 200 year period (1810 - 2010). It has been shown to suitably replicate observed decadal variation in wave heights (figure 4.12) whilst representing maximum observed wave heights (table 4.5) and is therefore suitable for use in this study.

4.3.2.4 Developing historical sea level data

As discussed in chapter 3, sea level is a major driver of coastal erosion. Furthermore, the nodal and tidal cycles of sea level complicate the delivery of wave energy to the foot of the cliff. Large wave heights occurring at neap tides may be less effective at delivering

	Observed Data (m)	Modelling Data (m)
Minimum	0	0
Maximum	13	13.81
Mean	1.38	1.38
Median	1	1.15
St. Deviation	1.04	1.58

TABLE 4.5: Descriptive statistics of observed hourly significant wave height series from the CLV between 1993 - 1999 and modelled hourly significant wave height series over the same period.

energy to the cliff foot than low wave heights occurring at spring tides. Therefore the cyclical variations, as well as long term trends, in sea level are important factors when considering energy delivery to cliffs.

Haigh *et al.* (2009a,b, 2010) have shown how sea level in the English Channel has changed over the past 100 years; rising at 1.19 ± 0.24 mm/yr in Southampton. They provide a record of hourly sea-level for Southampton which covers the period 1935 to present (Haigh *et al.*, 2009a). Unfortunately, this record does not cover the period required for this study (1810 - 2010) and therefore an extension of this record is required.

To extend the Southampton sea level record back in time, the long term record from Brest, France, is used. Hourly recordings of sea level have been recorded at Brest (48° 23' N, 004° 30' W) since 1846, making this record on of the longest hourly sea level records in the World. In order to extend the Southampton record using the Brest data, the linear relationship between the sea level records observed at the two sites over the period 1961 - 1990 was calculated. It was found that the records showed medium levels of correlation (Pearson's correlation coefficient = 0.4, $p < 0.05$), suggesting similar behaviour is recorded in both data sets. The relationship between the Brest and Southampton data over the calibration period was

$$\text{Southampton} = 3.905 - (0.261 \times \text{Brest}) \tag{4.20}$$

An r^2 of 0.38 suggests that although a large portion of the hourly variability within the data sets is not modelled, a substantial portion is explained by the values recorded at Brest. Therefore, this relationship was deemed valid for application to the rest of the Brest record.

In order to ensure the relationship detailed in Eq. 4.20 provided suitable values for Southampton sea level, the period 1935 - 1960 was used as a validation. The Brest data for this period was converted using Eq. 4.20 and compared to the corresponding observed data from Southampton. It was found that Eq. 4.20 produces acceptable values of Southampton sea level, with the Pearson's correlation coefficient between the modelled and observed data sets being 0.82 ($p < 0.05$) when applied to moving average low-pass

filtered data (figure 4.13a). This implies that the large scale trends in the observed data are replicated in the modelled data series.

Analysis of the residuals of the modelled and observed data (figure 4.13b) suggest there is no systematic under- or over-estimation. The mean of the residuals, -0.0063 suggests an ever so slight under-estimation within the modelled data. However, as this value is negligible the model is deemed to accurately represent the variability in the observed sea level climate. The maximum variability observed in the residuals is -0.06, as this value is safely within the natural variability of the observed data this is deemed suitable for this study. Therefore, the linear relationship described in Eq. 4.20 was deemed appropriate for use in extending the Southampton sea level record back to 1846. By applying Eq. 4.20 to the long term Brest record over the period 1846 - 1935 it is possible to extent the 1935 - 2010 Southampton record back to 1846. However, a record to 1810 is required. To get a data set covering the period 1810 to 1846, the Brest record for the period 1850 to 1886 was copied and appended to the beginning of the hourly sea level record from Brest. Eq. 4.20 was then applied to the 1810 to 1935 Brest record, and the results appended to the observed Southampton record to provide a hourly sea level series for the period 1810 - 2009 (figure 4.14).

As with the wave height series developed in section 4.3.2.3, the Hanna *et al.* (2008) pressure record from Jersey is used to assess the applicability of the long term sea level record (figure 4.14). As can be seen in figure 4.14, the synthesised long-term sea level record displays periods of quiescence and intensity over similar periodicities as those identified in the pressure change record. For example, the period between 1910 and 1930 is characterised by a high pressure and a corresponding lull in the mean wave heights. Similarly the lull in the Hanna *et al.* (2008) pressure record at 1990 corresponds to a period of higher mean average sea levels. As such, it can be said that the generated sea level record represents a plausible record for the 200 year period (1810 - 2010).

The final input for MT-CHILD model consists of one input file describing the wave climate of the study area. Accordingly, the wave height record produced in section 4.3.2.3 is combined to the sea level record produced here to provide a plausible historical record of overall wave heights which will model the variation in energy delivery to the cliff foot, accounting for nodal and tidal cycles in sea level and late twentieth century sea level rise.

4.3.3 Results and discussion

To determine whether MT-CHILD is able to model the development of Shepherds Chine from 1810 to the present, a series of metrics were employed to compare the model outputs against observations for model assessment. Following Leyland (2009) the metrics used to describe the observed form of Shepherds Chine include the gully mouth elevation, (m, GME), the width to depth ratio (W/D ratio) at the mouth of the Chine, the mean bank angle (°) at the gully mouth and the gully area (km^2). Definitions of the

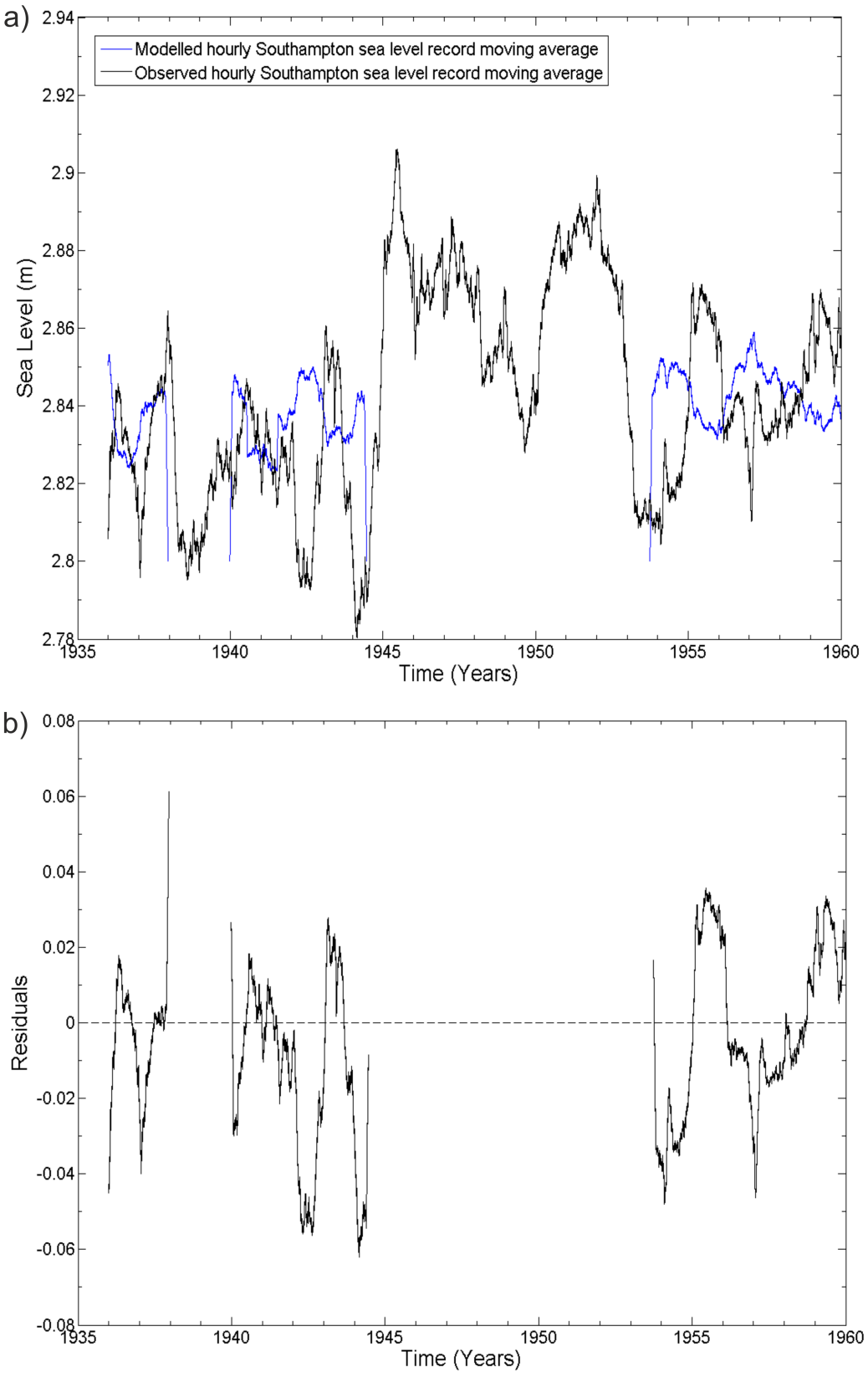

FIGURE 4.13: a) Yearly moving average of observed hourly sea level from Southampton the period 1935 - 1960 (black) and yearly moving average of the modelled hourly sea level record derived Eq. 4.20 based on hourly sea level from Brest over the same period. b) Residuals of modelled yearly moving average minus observed yearly moving average for the period 1935 - 1960. Gaps in data represent gaps in the Brest data.

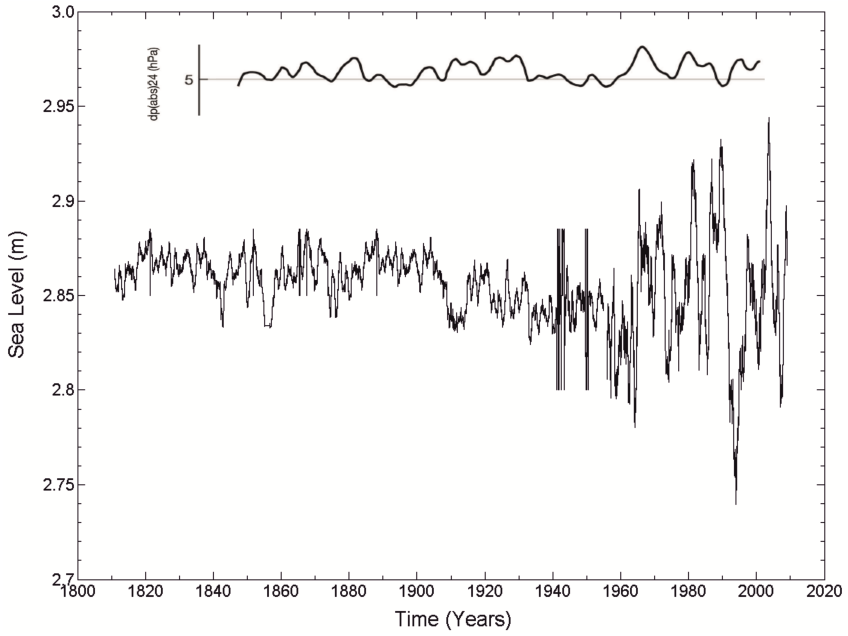

FIGURE 4.14: Yearly moving average of 200 year sea level record for Southampton created from a combination of modelled data from the Brest sea level record using Eq. 4.20 (1810 - 1935) and observed Southampton sea level (1935 to 2010). Peaks in moving average between 1940 to 1950 represent the transition to the more variable observed Southampton record. Inset is Hanna et al. (2008) pressure change (dp(abs)24, hPa) record for Jersey, acting as a storminess proxy for the English Channel. Data begins and ends 10 years earlier and later than actual series because of the nature of the 10 year moving average window.

metrics are provided in figure 4.15. The observed values are detailed in table 4.6.

Initially, MT-CHILD was parameterised using the values described in table 4.1 (labelled run *S1*, table 4.6). The synthesised historical rainfall and wave climates described in sections 4.3.2.2 and 4.3.2.3 were used as inputs for these respective variables. After the run was complete, the metrics detailed above were extracted from the final DEM. However, it was found that this parameterisation failed to replicate the required level of incision in Shepherds Chine (see table 4.6), leaving the elevation of the gully mouth too high. As the processes of bedrock erosion and, subsequently, incision ensure the headwards retreat of in-stream knickpoints, they are fundamental to the development of incised coastal gully systems (see section 2.1). Therefore, to ensure the correct parameterisation of this key process, a sensitivity analysis was conducted. As the level of incision with MT-CHILD is predominately controlled by the bedrock erodibility coefficient (K_B) the value of this parameter was adjusted until a suitable level of incision was modelled. All other input parameters were kept the same (i.e. as in table 4.1). A series of 9 further scenarios (named *S2* to *S10*) were conducted, with increasing values of K_B (see table 4.7).

For each of the 10 scenarios, the metrics described above were extracted from the final DEM for Shepherds Chine and recorded in table 4.7. To identify the scenario that best replicates the observed features, the values in table 4.7 were normalised by dividing the

	S1	S2	S3	S4	S5	S6	S7	S8	S9	S10
K_B	0.015	0.1	0.15	0.2	0.25	0.3	0.35	0.4	0.45	0.5
GME (m)	1.33	1.3	1.16	1.15	1.13	1.12	1.11	1.10	0.97	0.84
W/D Ratio	1.03	1.04	1.13	1.13	1.16	1.16	1.16	1.35	1.35	1.36
Gully Area (km^2)	0.67	0.67	0.66	0.66	0.64	0.64	0.63	0.62	0.61	0.60
Mean Bank Angle (°)	4.03	4.03	4.00	4.00	4.21	4.32	4.50	4.66	4.68	4.69
RMSE	3.49	3.51	3.51	3.56	3.67	3.75	3.86	4.14	4.23	4.36

TABLE 4.6: Normalised Chine metrics (observed / modelled values) of Shepherds Chine. Obsereved GME = 6 m, W/D ratio = 8.18, Gully area = 0.04km^2 and Mean Bank Angle = 20.36°. Values closer to one represent better model fit. K_B values represent the value of the bedrock erodibilty coefficient (K_B) used in the model run. Observed values were taken from 2009 LIDAR data. The width to depth ratio is taken at the mouth of the Chine. Root Mean Square Error (RMSE) provides an aggregated closeness of fit for each model scenario based on the non-normalised metric values.

	S2a	S2b	S2c	S2d	S2e	S2f	S2g	S2h	S2i	S2j	S2k	S2l	S2m	S2n	S2o	S2p
Critical Slope Gradient	0.5	0.6	0.7	0.8	0.9	1.0	1.1	1.2	1.3	1.4	1.5	1.6	1.7	1.8	1.9	2.0
GME (m)	1.50	1.33	1.24	1.15	1.11	1.10	1.10	1.10	1.00	1.00	0.98	0.98	0.97	0.97	0.97	0.97
W/D Ratio	1.15	1.15	1.21	1.09	1.09	1.02	1.02	0.97	0.95	0.96	1.01	1.05	1.02	1.09	1.02	1.02
Gully Area (km^2)	0.95	1.00	1.00	1.13	1.05	1.10	1.10	1.10	1.00	1.05	1.05	1.03	1.10	1.10	1.08	1.20
Mean Bank Angle (°)	0.828	0.837	0.842	0.840	0.841	0.840	0.843	0.840	0.840	0.840	0.843	0.843	0.843	0.843	0.843	0.844
RMSE	2.38	2.03	1.95	1.71	1.68	1.64	1.61	1.64	1.64	1.64	1.60	1.61	1.60	1.64	1.60	1.60

TABLE 4.7: Normalised Chine metrics (observed / modelled values) of Shepherds Chine. Obsereved GME = 6 m, W/D ratio = 8.18, Gully area = 0.04km^2 and Mean Bank Angle = 20.36°. Values closer to one represent better model fit. Critical slope gradient values represent value of the critical slope parameter used in the model run. Observed values were taken from 2009 LIDAR data. The width to depth ratio is taken at the mouth of the Chine. Root Mean Square Error (RMSE) provides an aggregated closeness of fit for each model scenario based on the non-normalised metric values.

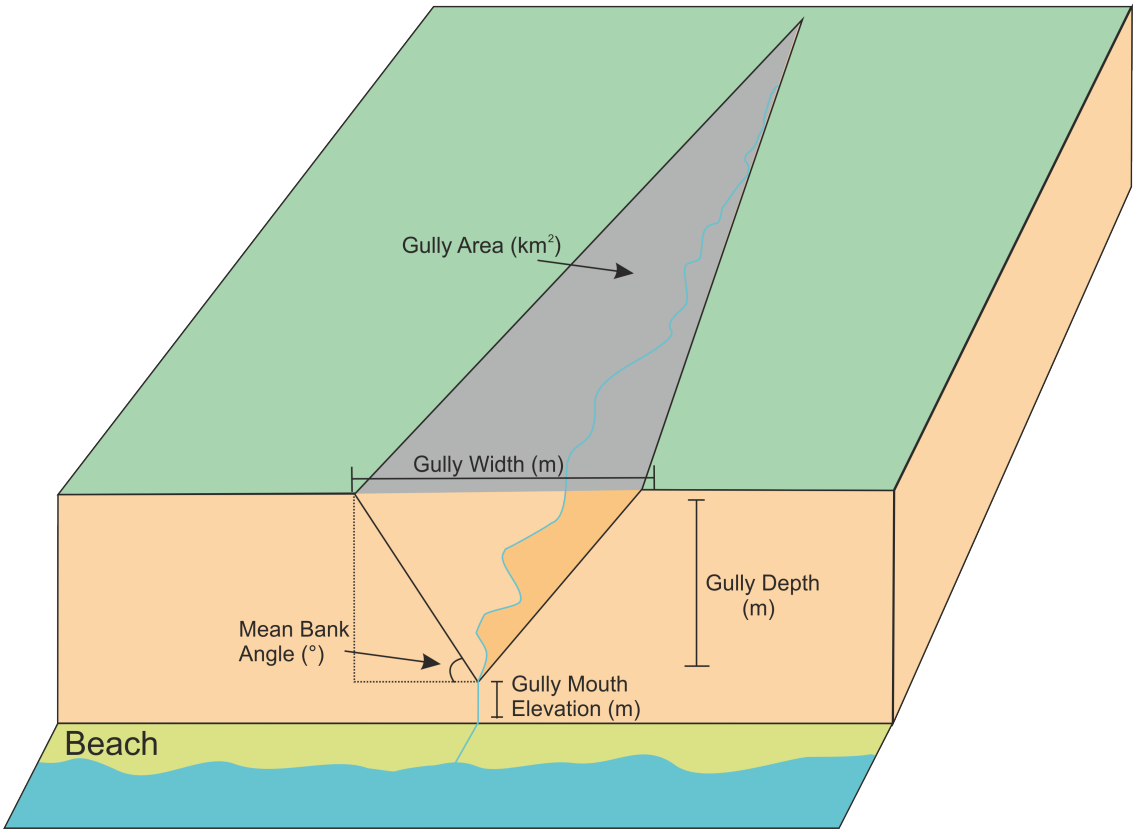

FIGURE 4.15: Definition diagram of the metrics used to assess the simulation of Shepherds Chine. The width to depth ratio is calculated from the gully width and gully depth as identified. The gully area (km^2) is the area of the grey shaded triangle area. Mean bank angles (°) are taken over a 10 m distance inland from the gully mouth.

modelled value by the observed value (figure 4.16). These normalised metrics therefore represent the deviation of the model output from the observed value (figure 4.16), with a value of unity indicating perfect agreement.

As can be seen in figure 4.16a, by increasing the bedrock erodibility coefficient the gully mouth elevation of Shepherds Chine drops, as rates of incision increase. Furthermore, the increase in bedrock erodibilty results in an increase in the gully area (figure 4.16c). This is due to the gullying and increased mass wasting of the gully sidewalls, induced by the higher erodibility coefficient. It can be seen in figure 4.16d that mean bank angles at the mouth of Shepherds Chine are consistently underestimated. Furthermore, the average bank angle at the gully mouth decreases with increasing erodibility, and thus incision. This is counter-intuitive, as an increase in incision rates (as seen by the decrease in gully mouth elevation in figure 4.16a) should result in steeper bank angles. This issue is also manifest in the width/depth ratio (figure 4.16b), which shows an increase with increasing erodibility. This is due to the mass wasting and collapse of the gully side walls, resulting in an over-widening of the gully at its mouth. It therefore appears that the parameter describing the critical slope for mass wasting (set at 0.75 for these runs) is wrongly parameterised. As the critical slope parameter is directly related to the amount and type of mass-wasting processes occurring at these locations (section

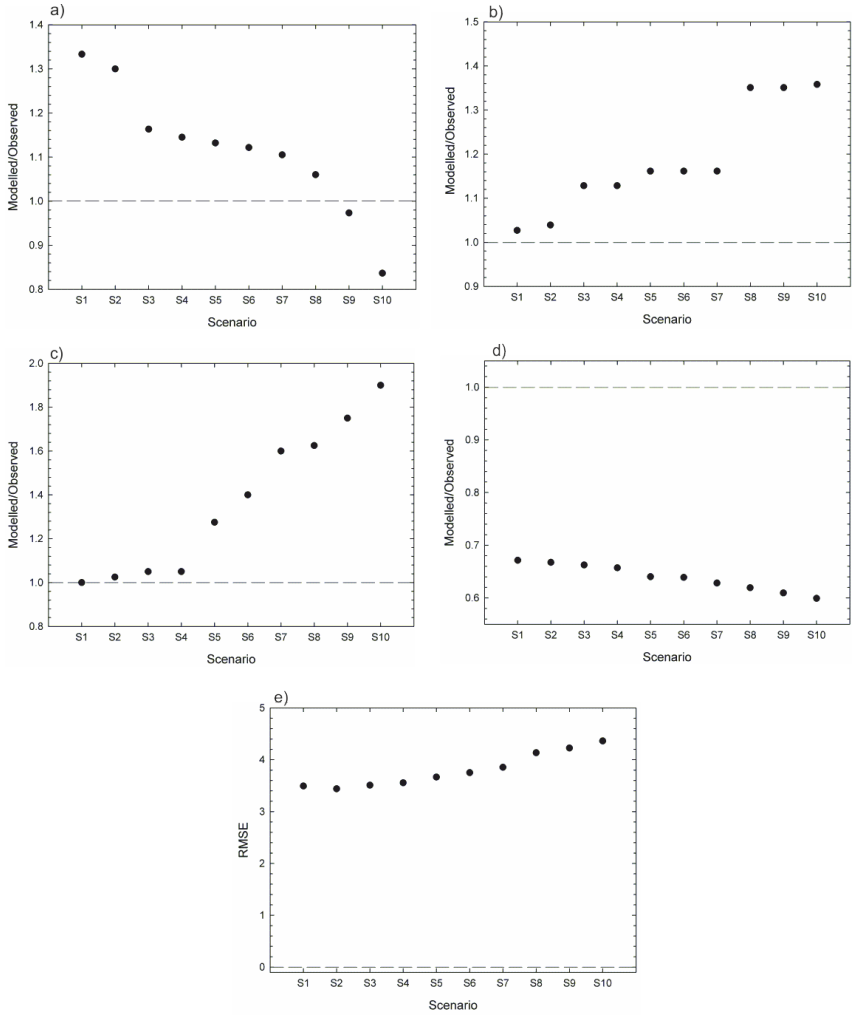

FIGURE 4.16: Ratios of modelled to observed metrics for a) gully mouth elevation, b) width to depth ratio, c) gully area and d) mean bank angle. Reference lines show the perfect fit between modelled and observed values. The Root Mean Square Error (RMSE) in figure e) is calculated from the combined raw values of the metrics, and represents the total deviation from the observed landform for each model scenario. Scenarios *S1* to *S10* represent increase bedrock erodibility coefficients.

4.1.4.1, Eq.4.4), the current value of 0.75 is evidently too small to maintain realistic gully side-wall angles within MT-CHILD.

To determine which of the scenarios modelled above (figure 4.16) best represents the observed features along the south west Isle of Wight, a single metric of fit is required within which the multiple variables, or metrics, can be aggregated. Furthermore, it is necessary that the optimisation gives equal weight to each of the metrics taken. Accordingly, the Root Mean Square Error (RMSE) for each scenario was calculated (figure 4.16e) from the raw, non-normalised, metric values. The scenario which best replicated the observed features is the scenario with the RMSE closest to zero. As can be seen in figure 4.16e, all the scenarios differ from the observed landforms. The deviation from the observed values increases as the bedrock erodibility coefficient increases, suggesting that lower bedrock erodibility coefficients more closely represent the current

gully features. By looking at individual metrics, bank angle displays the greatest deviation from the observed features, and contributes most to the large RMSE values observed. This further justifies the need to better constrain the critical bank angle parameter. To do this, the scenario which best replicates the observed features was chosen as a base scenario for an additional sensitivity analysis for the critical slope. Figure 4.16e suggests that this is scenario *S2* (K_B = 0.1; RMSE = 3.2).

To further test the importance of the critical angle on the metrics and formation of the gully landforms, MT-CHILD was parameterised as scenario *S2* but with a varying critical slope value. The critical slope value was varied from 0.5 to 2 at 0.1 intervals. This resulted in 16 scenarios labelled *S2a* to *S2p*. By varying the critical slope value, it is hoped that the deviation from the observed landform shown in scenario *S2* will be constrained and reduced, resulting in a closer match to reality. Results are described in table 4.8. The results were then normalised by dividing the modelled outputs against the observed outputs (figure 4.16). Initially it can be seen, that there is still large variation between the separate scenarios, however the modelled metrics more closely represent those in reality than previous runs. Gully mouth elevation converges around the observed value as critical slope angle increases (figure 4.17a).

Mean gully bank angles are still consistently underestimated within MT-CHILD (figure 4.17d). This may indicate a lack of appropriate process representation within the model. However, by increasing the critical slope gradient (S_c; Eq.4.4), bank angles increase towards the observed values. Scenarios with larger S_c values also produce bank angles which are more realistic than those shown in figure 4.16d, with the modelled to observed ratio being ∼0.84 rather than ∼0.74. The discrepancy in the bank angle still manifests itself in the overall RMSE for each scenario (figure 4.17e). However, as S_c increases, the RMSE decreases. This suggests that by increasing S_c, it is possible to better constrain and replicate observed incised coastal gully landforms. Furthermore, the RMSE values displayed in figure 4.17e (in the range 1.6 to 2.4), are a lot closer to unity than those shown in figure 4.16e (of the range 3.5 to 4.5). The best set of parameters based on the RMSE values for the combined metrics (figure 4.16e) are scenario *S2m* (RMSE = 1.5990), *S2o* (RMSE = 1.5999) and *S2p* (RMSE = 1.5999). These correspond to a S_c value of 1.7 (59.5°), 1.9 (62.2°) and 2.0 (63.4°), respectively. These scenarios also correspond to the three scenarios whose mean bank angle at the gully mouth was the closest to the observed (17.2° in all three cases).

It should be noted that the critical slope angles are necessarily high when compared to observed bank angles as this value represents the angle at which sediment flux becomes infinite see Eq.4.4. As such, slopes of this angle should not be observable in the field because as flux tends to infinity, such slopes would rapidly decline (Roering *et al.*, 1999, 2001). Therefore, as such high values of critical slope angle have been shown to produce the most realistic bank angles at the gully mouth, their application is theoretically justified. Observed bank angles proposed by Leyland and Darby (2008) in the Channel Evolution Model (CEM; figure 4.18), suggest bank angles of 3.8° ± 4.2° to 34.5° ± 3.9°

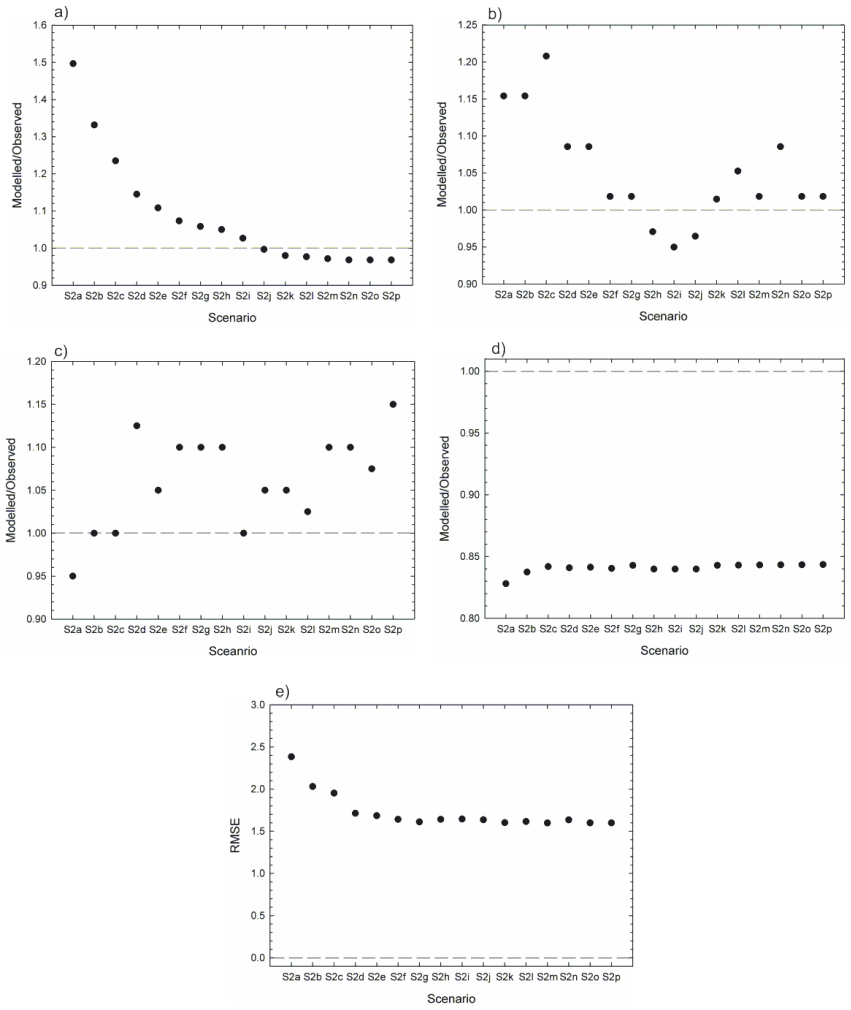

FIGURE 4.17: Ratios of modelled to observed metrics for a) gully mouth elevation, b) width to depth ratio, c) gully area and d) mean bank angle. Reference lines show the perfect fit between modelled and observed values. The Root Mean Square Error (RMSE) in figure e) is calculated from the combined raw metric values, and represents the total deviation from the observed landform for each model scenario.

in stage V in Wealden Shales and Marls, and bank angles of 16.3° ± 4.9° to 57.9° ± 8.5° in Lower Greensands. Modelled bank angles are in the range 16.86° to 17.17°, so fall in the lower end of the observed bank angles, however are still within the range of observed angles.

Of the three scenarios which best describe the formation of Shepherds Chine (*S2m*, *S2o* and *S2p*), scenario *S2m* has the lowest RMSE (1.5990). The difference in RMSE is very small between the three sceanrios (0.009). Furthermore, considering that the measured bank angles are the same for all three of these scenarios (17.2°), despite differing critical slope angles, all three scenarios mentioned above produce very similar outputs. For the sake of the lower RMSE value and that this scenario produced bank angles which are the closest 'best fit' to prior studies (e.g. Leyland and Darby, 2008), the set of parameters comprising scenario *S2m* (table 4.8) is chosen as the parameter set which best describes the development of Shepherds Chine since 1810.

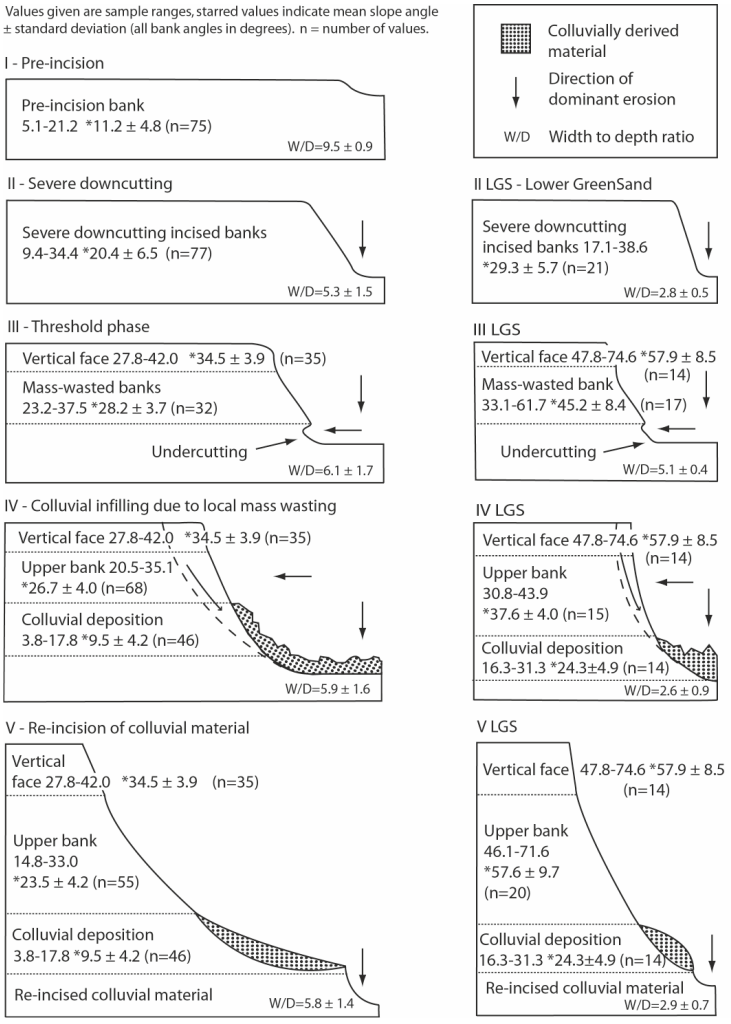

FIGURE 4.18: Bank slope development characteristics associated with the five stages of the Leyland and Darby (2008) CEM for incised coastal gullies. Note scale is relevant. From Leyland Darby (2008), their figure 7.

In order to assess the success of parameter set *S2m* in replicating observed channel forms, stream profiles were extracted from each model timestep (output every 10 years, resulting in 20 profiles). These profiles begin ∼10 m from the headcut of the gully and extend downstream until base-level is reached. The resultant profiles are compared to the observed channel stream profile (figure 4.19) to enable a assessment of the development of knickpoint and channel elevations across the model simulation. As can be seen in figure 4.19 modelled and observed rates of cliff retreat agree with each other (~ 0.5 m^{-1}). However, larger discrepancies occur in the rates of knickpoint recession. In figure 4.19 a knickpoint close to the mouth of the stream profile is tracked back through the model simulation; representing the progression of this knickpoint through the gully system. The rate of this knickpoint's retreat is 0.49 ma^{-1}. By comparison, the estimated observed value for knickpoint recession rates in Shepherds Chine are ∼0.96 ma^{-1} (Leyland and Darby, 2008). It should be noted that there are no actual observed measurement of knickpoint recession rates over the 190 year simulation period. The values provided by (Leyland and Darby, 2008) are an estimate based on the assumption

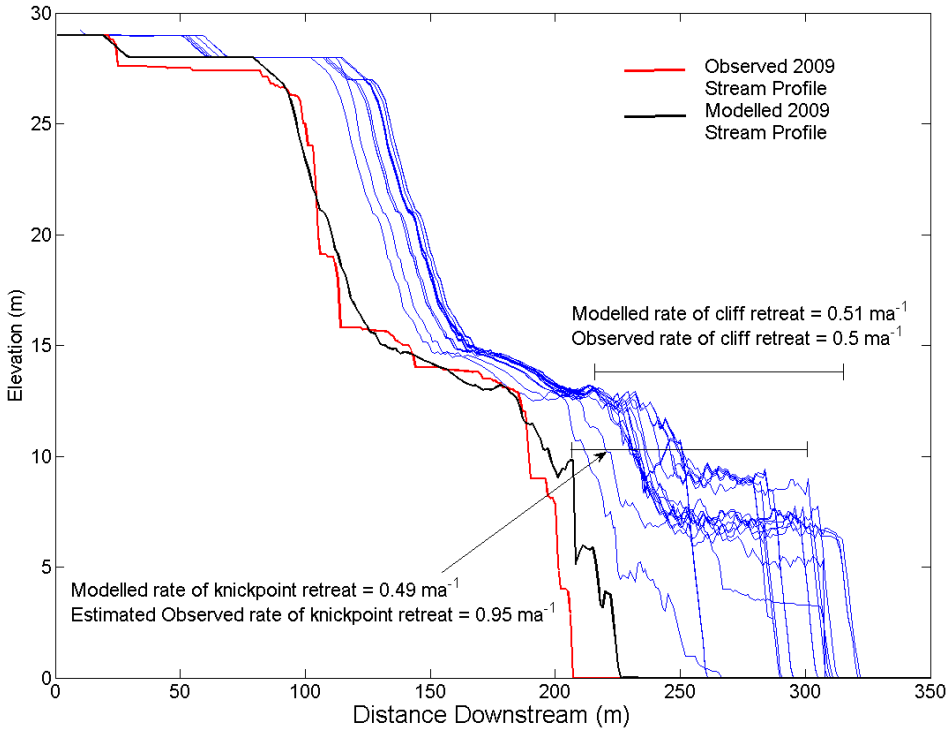

FIGURE 4.19: Modelled and observed stream profiles of Shepherds Chine. Modelled stream profiles are output every 10 years (in blue). The final model output is shown in black and the observed stream profile of Shepherds Chine is shown in red.

that a knickpoint within the current profile of the Shepherds Chine system was formed during a large storm in 1703. There is no confirmation of this assumption, it is therefore possible that the values suggested by Leyland and Darby (2008) are inaccurate and not representative of knickpoint rates within the gully systems. As can be seen in figure 4.19 the profiles evolve throughout the simulation period towards the observed stream profile. The presence of a step at the mouth of the gully early in the simulation is a artefact of the manual cutting of this section of the channel due to the extension of the DEM (see section 4.3.2.1 for details). This step is removed as the simulation develops and the stream profile converges on the observed profile. This provides confidence that MT-CHILD is able to replicate the processes of gully development and the interaction between coastal and terrestrial processes.

A further assessment of MT-CHILDs skill in replicating observed gully forms is provided through analysis of channel cross-sections. Cross-sections were taken at the mouth of the gully, where the width/depth metric described earlier was calculated. This is one of the most active areas of the gully, as well as being the most influenced by both marine and terrestrial processes, therefore by taking the cross-sections in this location, the ability of MT-CHILD to replicate and model active gully sidewalls is assessed. Figure 4.20 shows that the gully sidewalls in Shepherds Chine widen across the 190 year period. This is consistent with the Leyland and Darby (2008) CEM (section 2.2.1 and figure 2.2) which

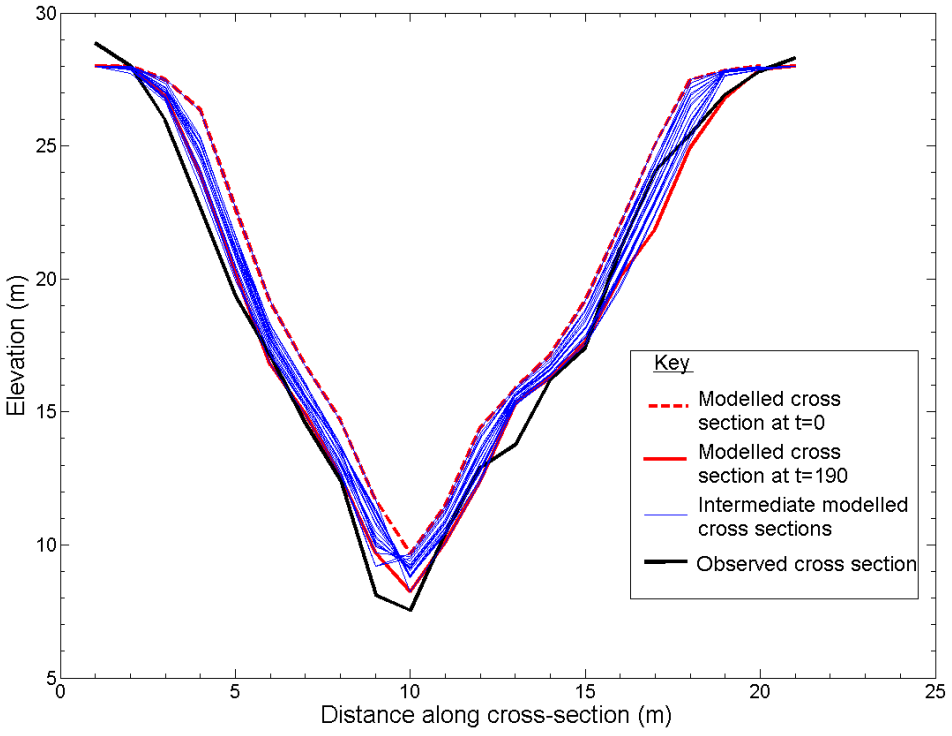

FIGURE 4.20: Modelled and observed cross-sectional profiles of Shepherds Chine. Modelled cross-sections are shown for every 10 years of the model simulation (blue). The initial model cross-section is depicted by the dashed red line. The final model cross-section is depicted by a solid red line and the observed Shepherds Chine cross-section is shown by the black solid line

shows a widening and incision towards the mouth of gully systems. As can be seen in figure 4.20 the gully incises through the model simulation period until the final bed elevation is only slightly higher (∼1 m)than the observed cross-section. The profile of the side-walls is maintained throughout the simulation suggesting mass-movement processes are not eroding the gully sides away to unrealistic profiles. This provides confidence in MT-CHILDs ability to model terrestrial, hillslope processes. Although not a perfect fit, the final model cross-section bares resemblance to the observed cross-section, suggesting MT-CHILD is capable of maintaining gully sidewall profiles in the most active part of the gully, whilst modelling bedrock incision and bed elevation lowering.

Visual comparison of the *S2m* output and aerial photos (figure 4.21) suggests that parameter set *S2m* is capable of replicating observed landforms, albeit with some errors. Features such as the A3055 road (seen at the top of figure 4.21b) and the Atherfield Bay Holiday camp infrastructure (middle of figure 4.21b) provide permanent structures useful for identifying areas where the model may over- or under-estimate erosion or deposition. It can be seen that the course of Shepherds Chine deviates from the observed course in the shaded area in figure 4.21. This is a remnant of the re-interpolation technique used after the current DEM was extended to the 1810 position (see section 4.3.2.1 for details). This technique resulted in the cut portion of the DEM being moved down to the 1810

Parameter	Units	Value
Fluvial Erosion		
K_f - regolith transoprt efficiency	n/a	1
K_w - hydraulic width coefficient	n/a	10
w_b - hydraulic width exponent	n/a	0.5
τ_{cr} - critical shear stress (Wealden Shales and Marls)	Nm^{-2}	3.6
τ_{cr} - critical shear stress (Lower Greensands)	Nm^{-2}	1.8
Bedrock Erosion		
K_{br} - bedrock erodibility coefficient	L^{1-2m}/T	0.1
P_b - critical shear stress exponent	n/a	1.5
τ_{cr} - critical shear stress (Wealden Shales and Marls)	Nm^{-2}	3.6
τ_{cr} - critical shear stress (Lower Greensands)	Nm^{-2}	1.8
Hillslope Erosion		
K_d - hillslope diffusivity coefficient	ma^{-1}	0.01
S_c - critical slope for mass wasting	m/m	1.7

TABLE 4.8: Summary of parameter values from scenario *S2m*, chosen as the best parameter set to describe the development of Shepherds Chine since 1810.

shoreline position to preserve the position of the gully mouth, rather than being adjusted laterally to preserve the shape of the gully channel. This technique was chosen as it minimised model errors which would have been larger had the gully not have developed in a similar area to the observed feature. As such, this deviation does not represent an error in the model flow routing processes.

It can also be seen that the side walls of both Chines have developed smaller gully networks. Conversely, on the aerial image limited gullying of the side wall is present. This may suggest that the bedrock erodibility parameter is set too low, as more erosion is occurring than in reality. It may, however, be symptomatic of the under-representation of the influence of vegetation within the model. Vegetation acts as a resistor to gully development (Kirkby and Bull, 2000; Kirkby *et al.*, 2003; Poesen *et al.*, 2003; Istanbulluoglu *et al.*, 2005; Valentin *et al.*, 2005), effectively increasing the erodibility coefficient of the model (Istanbulluoglu *et al.*, 2005) and reducing the presence of hillslope gullies. The presence of increased side wall gullying suggests that the MT-CHILD is not parameterised to model the effects of the low-lying gully side wall vegetation. However, as shown in figure 4.17, scenario *S2m* is able to recreate realistic width to depth ratios and gully areas, therefore the presence of these side wall gully networks appears to have a minimal effect on the metrics taken. Recognising this fact, the development of side wall gully networks presents an acceptable deviation from the observed feature and does not produce large errors when gully metrics are taken.

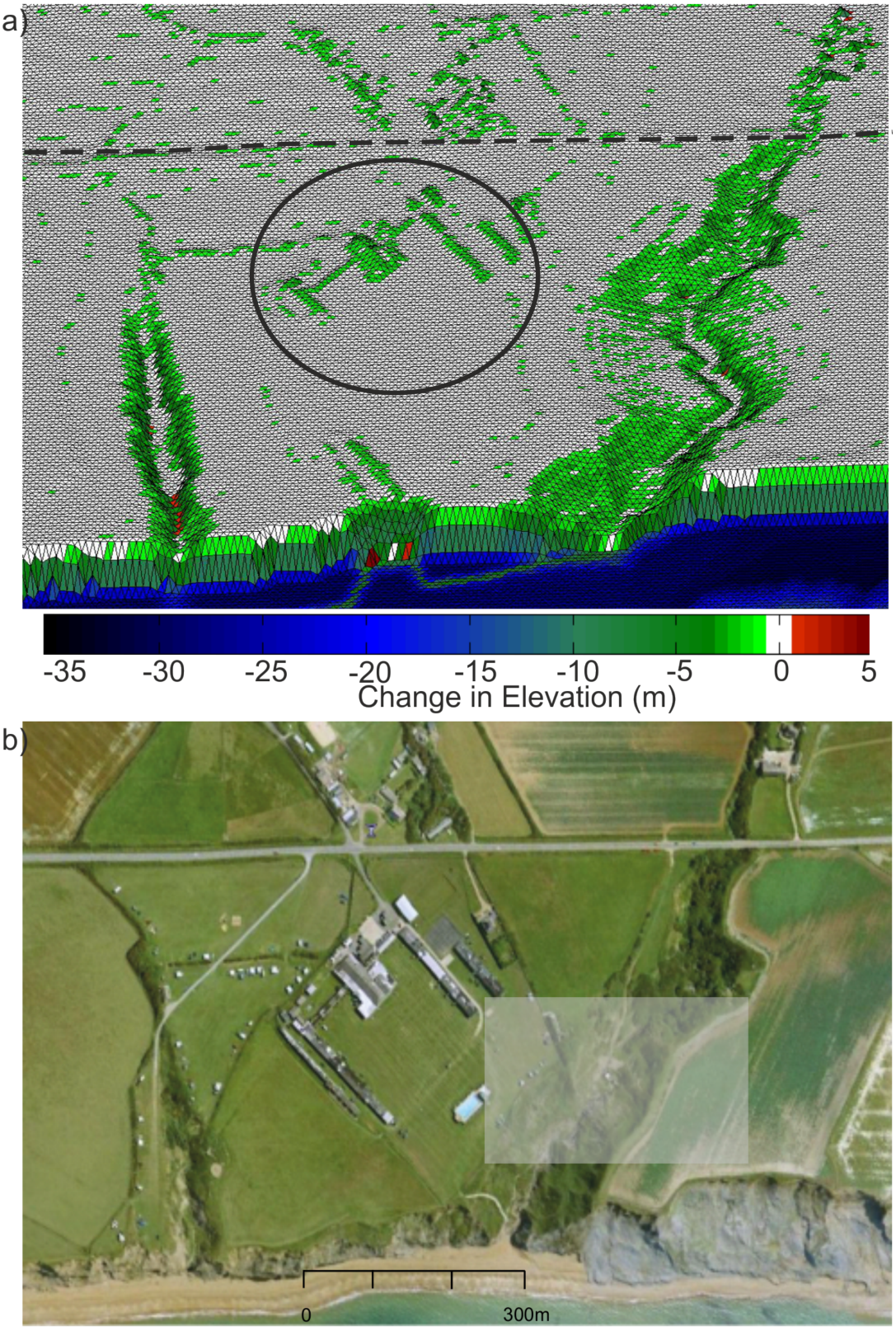

FIGURE 4.21: a) MT-CHILD output of model scenario S2m showing change in elevation (m) from 1810 to present. Cowleaze Chine is on the left and Shepherds is on the right. b) Aerial image of Cowleaze (left) and Shepherds (right) Chine. The A3055 road seen at the top of b) is highlighted by the dashed line in a), likewise the structure of the holiday camp visible in the middle of b) is circled in a). The shaded area in a) and b) represents the area where the model gully course deviates from the observed gully course.

4.4 Conclusion

It has been shown above that a process-based model of soft cliff erosion (developed in chapter 3) can be incorporated into the terrestrial landscape evolution model CHILD. The modified version of CHILD presented above represents the first fully integrated marine-terrestrial LEM capable of modelling the interactions between processes of coastal erosion and terrestrial landscape evolution (i.e. fluvial and hillslope erosion).

Validation of the model suggests that given the correct parameter set up (detailed in table 4.8), the model is able to recreate the historic development of Shepherds Chine over the period 1810 to present. It is therefore possible to infer that the modified CHILD LEM is able to model the complex interactions between coastal and terrestrial processes upon such dynamic features as the incised coastal gullies of the Isle of Wight. Moreover, this model has the ability to be applied to other systems which are driven by the interaction between coastal and terrestrial processes (e.g. rivers debouching at the coast) or to systems which are purely driven by cliff retreat processes (e.g. unbroken cliff faces). Furthermore, the validation process has provided a parameter set which has been shown to accurately model the development of incised coastal gullies over a ca. 200 year period (*S2m*, table 4.8). Therefore, by modifying the input files and input DEM, it should be possible to assess the impacts that sea level rise, changing wave climates and precipitation regimes may have upon these features in the future (assuming accurate future projections of sea level, wave and atmospheric climate regimes). It is these changes in driving forces, and possible scenarios of future climate change, which shall be developed in chapter 5.